

Inverse-Compton Emission from Clusters of Galaxies: Predictions for ASTRO-H

Richard Bartels, Fabio Zandanel, and Shin'ichiro Ando

GRAPPA Institute, University of Amsterdam, 1098XH Amsterdam, The Netherlands
e-mail: r.t.bartels@uva.nl

Received 00 00, 0000; accepted 00 00, 0000

ABSTRACT

The intra-cluster medium of several galaxy clusters hosts large-scale regions of diffuse synchrotron radio emission, known as radio halos and relics, which demonstrate the presence of magnetic fields and relativistic electrons in clusters. These relativistic electrons should also emit X-rays through inverse-Compton scattering off of cosmic microwave background photons. The detection of such a non-thermal X-ray component, together with the radio measurement, would permit to clearly separate the magnetic field from the relativistic electron distribution as the inverse-Compton emission is independent from the magnetic field in the cluster. However, non-thermal X-rays have not been conclusively detected from any cluster of galaxies so far. In this paper, for the first time, we model the synchrotron and inverse-Compton emission of all clusters hosting radio halos and relics for which the spectral index can be determined. We provide constraints on the volume-average magnetic field by comparing with current X-ray measurements. We then estimate the maximum volume-average magnetic field that will allow the detection of inverse-Compton hard X-rays by the ASTRO-H satellite. We found that several clusters are good targets for ASTRO-H to detect their inverse-Compton emission, in particular that corresponding to radio relics, and propose a list of promising targets for which ASTRO-H can test $\geq 1 \mu\text{G}$ magnetic fields. We conclude that future hard X-ray observations by the already-operating NuSTAR and the soon-to-be-launched ASTRO-H definitely have the potential to shed light on the long-sought non-thermal hard-X-ray emission in clusters of galaxies.

Key words. Galaxies: clusters: intracluster medium – Magnetic fields – Radiation mechanisms: non-thermal – Radio continuum: general – X-rays: galaxies: clusters

1. Introduction

The observation of diffuse synchrotron emission in clusters of galaxies proves the presence of magnetic fields and relativistic electrons in the intra-cluster medium (ICM). This diffuse radio emission is observationally classified into two phenomena: peripheral radio relics that show irregular morphology and appear to trace merger and accretion shocks, and radio halos centred on clusters showing a regular morphology resembling that of the thermal X-ray emission (e.g., Feretti et al., 2012).

The electrons generating the observed radio emission can also produce X-rays by inverse-Compton (IC) scattering off of cosmic microwave background (CMB) photons. IC emission has been searched for extensively in the past, with a few claims of detection (see, e.g., Rephaeli & Gruber, 2002; Fusco-Femiano et al., 2004; Rephaeli et al., 2006; Eckert et al., 2008; Rephaeli et al., 2008). However, more recent observations did not confirm most of the earlier claims (Molendi & Gastaldello, 2009; Ajello et al., 2009, 2010; Wik et al., 2012; Ota, 2012; Ota et al., 2014; Wik et al., 2014; Gastaldello et al., 2015) and IC emission from clusters remains elusive.

The dominant emission in clusters of galaxies is the thermal bremsstrahlung from the ICM. Since this falls quickly above ~ 10 keV, hard X-rays (HXR) offer the best prospect for detecting IC emission from clusters. In the coming years, next generation X-ray satellites will increase the chances. Especially, ASTRO-H (Takahashi et al., 2012, 2014; Kitayama et al., 2014), to be launched this year (2015), and the recently launched NuSTAR (Harrison et al., 2013) are excellent instruments to probe IC emission in HXR.

In this work, we model, for the first time, the synchrotron and IC emission of *all galaxy clusters hosting radio halos and relics* for which the spectral index can be determined. The radio-emitting electrons in clusters can be of different origin (see, e.g., Brunetti & Jones, 2014 for a review). Our approach is phenomenological, we do not make any assumption on the injection and acceleration history of the relativistic electrons, and we only assume that the same electron distribution generating the observed synchrotron radio emission, IC scatter off of the CMB photons. We compare with current X-ray observations, where available, and provide detailed predictions for the ASTRO-H satellite. In particular, we estimate cap values for the volume-averaged magnetic field below which an IC signal would be detectable by ASTRO-H.

The detection of IC emission from clusters of galaxies is crucial to break the degeneracy in the determination of the electron distribution and magnetic field value in clusters. As the synchrotron radio emission depends on both, while the IC emission is independent of the cluster's magnetic field, the detection of the latter in HXR is of fundamental importance. This not only will shed new light on non-thermal emission in clusters, but also on the impact of non-thermal phenomena on the thermal content of galaxy clusters, which is fundamental in order to robustly use galaxy clusters for cosmological studies (Voit, 2005).

This paper is organised as follows. We introduce our sample of radio halos and relics in Section 2 and describe how we treat the relativistic electrons in Section 3. In Section 4, we briefly discuss how the non-thermal synchrotron and IC emission is modelled, while, in Section 5, we discuss the considered background emissions. We describe the main characteristics of

the ASTRO-H satellite that are of importance for this work in Section 6, and explain the procedures adopted for determining the IC detectability by ASTRO-H in Section 7. Eventually, we present all results in Section 8. We present our conclusions in Section 9. We work in cgs units and adopt a cosmological model with $\Omega_m = 0.27$, $\Omega_\Lambda = 0.73$ and $H_0 = 70 \text{ km s}^{-1} \text{ Mpc}^{-1}$.

2. Galaxy cluster sample

We analyse the radio halos and relics from the *September2011-Halo* and *September2011-Relic* collections of Feretti et al. (2012). We limit our final sample to objects that have at least two radio measurements at different wavelengths in order to be able to determine the corresponding photon spectral index α and reduce the degeneracy in our modelling. There are a few sources for which the spectral index was estimated from neighbouring wavelengths being subject to a uncertainty and are therefore excluded from our sample (A545 halo, A115 and A548 relics). Additionally, we searched the literature for radio data published after Feretti et al. (2012) which led to the inclusion of the Toothbrush (1RXS J0603.3+4214), A3376, A3411, A3667 south-eastern relic, El-Gordo (ACT-CL J0102-4915), MACSJ1149.5+2223, MACSJ1752.0+4440, PLCK G171.9-40.7 and ZwCl2341.1+0000 in our final sample.

We exclude from the present analysis radio mini-halos hosted in cool-core clusters as the magnetic field estimates in the centre of these environments are high, up to $\sim 10 \mu\text{G}$ (Clarke, 2004; Enßlin & Vogt, 2006), implying very low relativistic electron densities for which it would be extremely difficult to aim for a IC detection.¹ Table 1 and 2 contain the information regarding our sample of radio halos and relics, respectively, including current X-ray upper limits where available. A note on the latter: most of current HXR upper limits come from observations pointed at the center of clusters; there are a just few works dedicated to radio relics. In most cases, these HXR upper limits contain contributions from both halo and relic regions.

3. The electron population distribution

As anticipated above, we take a phenomenological approach regarding the radio-emitting electrons. We assume a power-law distribution of electrons,

$$N(\gamma, \theta) = K_0 \gamma^{-(2\alpha+1)} \frac{\sin \theta}{2}, \quad (1)$$

with K_0 the normalisation, γ the Lorentz factor and α the photon spectral index, where we consider an isotropic distribution of pitch angles θ . The electron distribution is then integrated between γ_{\min} and γ_{\max} . In some of the analysed cases, where spectral steepening is clearly observed, γ_{\min} and γ_{\max} can be determined from the radio data. However, more often there is no evidence for such feature, in which case the cutoffs are fixed to theoretically motivated values.

The low energy cutoff is estimated from the lifetime of relativistic electrons in the ICM. At low energies ($\gamma \lesssim 10^2$) Coulomb cooling dominates, whereas at high energies IC cooling dominates (Rephaeli, 1979; Sarazin, 1999). For typical values in the center of clusters, i.e., a thermal electron number density of $n_e \sim 10^{-3} \text{ cm}^{-3}$ and $B = 1 \mu\text{G}$, this yields a maximum lifetime

¹ See, however, Eckert et al. (2008), Pérez-Torres et al. (2009) and Murgia et al. (2010) for the case of the Ophiuchus galaxy cluster, hosting a radio mini-halo, for which the detection of non-thermal HXR emission has been claimed.

of $\gamma \approx 300$. However, outskirts of the cluster are characterised by lower ICM densities which implies $\gamma \approx 200$. Therefore, the low energy cutoff is fixed to $\gamma_{\min} = 300$ for halos, and to 200 for relics. The high-energy cutoff γ_{\max} is more arbitrary given that we do not make assumptions on the injection and acceleration history of the radio-emitting electrons. If no spectral steepening at high radio frequencies is observed, it is fixed to $\gamma_{\max} = 2 \times 10^5$, corresponding to electron energies of 100 GeV. Anyhow, as we will also show in Sect. 8, our conclusions are not affected by changing γ_{\min} and/or γ_{\max} , unless, of course, spectral steepening is observed.

4. Radiative processes

In this work, we assume that the magnetic field is tangled on scales much smaller than the observed emitting volume, therefore, adopting an isotropic distribution of magnetic field orientations. Such a distribution is well motivated by Faraday rotation (FR) measurements in clusters, which indicate that the coherence scales of magnetic fields are of the order 10 kpc, much smaller than the typical Mpc-size of radio halos and relics (Carilli & Taylor, 2002; Murgia et al., 2004, 2010). The synchrotron flux density is then given by

$$S_{\text{SYNC}} = \frac{V}{4\pi D_L^2} \int_{\gamma_{\min}}^{\gamma_{\max}} \int_0^\pi P(\nu, \gamma, \theta) N(\gamma, \theta) \frac{\sin \theta}{2} d\gamma d\theta, \quad (2)$$

where $P(\nu, \gamma, \theta)$ is the synchrotron spectrum emitted by a single electron (Blumenthal & Gould, 1970), V is the emitting volume and D_L is the luminosity distance. Note that the factor $\sin \theta/2$ is due to our assumption on the magnetic field distribution. The presence of this factor leads to slightly higher estimates of the magnetic field with respect to assuming coherent magnetic fields on large scales (e.g., Wik et al., 2009, Ajello et al., 2009 and Ajello et al., 2010). This assumption of tangled magnetic fields releases part of the tension between the typically high FR measurements and equipartition estimates of the magnetic field on the one hand, and claimed IC detections on the other. Indeed, there are several uncertainties that affect magnetic field estimates from IC emission, and, therefore, the comparison with results from FR measurements. While some of these sources of uncertainties will be discussed in more detail in the next sections, we remind the reader to, e.g., Petrosian (2001), Brunetti (2003) and Bonafede et al. (2010) for extensive discussions.

Low-energy photons scattering off of relativistic electrons can produce X-rays through IC emission. We assume that all incoming photons are from the CMB.² While starlight at the very centre of galaxy clusters can be as important as the CMB, this is not true when considering larger areas, as the ones corresponding to radio halos, or the clusters' outskirts where radio relics lie (see, e.g., Pinzke et al., 2011). The IC flux density is then given by

$$S_{\text{IC}} = \frac{V}{4\pi D_L^2} \int_0^\infty \int_{\gamma_{\min}}^{\gamma_{\max}} N(\gamma) F_{\text{IC}}(\epsilon, \gamma, \epsilon_1) d\gamma d\epsilon, \quad (3)$$

where ϵ is the incoming photon energy, ϵ_1 is the outgoing photon energy, and F_{IC} is the IC kernel function (Blumenthal & Gould, 1970) for the Thomson limit, valid for the energy range of interest here. Note that here $N(\gamma) = \int_0^\pi N(\gamma, \theta) d\theta$.

We conclude this section with an estimate of which HXR IC energies correspond to electrons emitting synchrotron radiation at a given frequency. This depends on the magnetic field

² Note that synchrotron-self Comptonization is also possible (e.g., Enßlin & Sunyaev, 2002).

Table 1. Radio halo sample

Cluster	z	Size	$F_{X, UL}$	$\Delta E_{X, UL}$	Γ	APEC normalisation	kT	Ref. 1	Ref. 2	Ref. 3
Bullet	0.30	19	1.10	50-100	1.9	7.99×10^{-3}	11.7	1, 2	38	45
A0520	0.20	25				1.96×10^{-3}	4.4	3		45
A0521	0.25	20				2.58×10^{-3}	4.9	4, 5, 6		45
A0665	0.18	79	4.20	0.6-7	1.6	8.48×10^{-3}	6.8	7	39	45
A0697	0.28	20				1.37×10^{-1}	8.8	6, 8		45
A0754	0.05	57	6.50	50-100	2.0	3.73×10^{-2}	9.0	9, 10	40	46
A1300	0.31	18				2.78×10^{-3}	6.3	11		45
Coma	0.02	710	4.20	20-80	2.0	2.18×10^{-1}	8.4	12	41	46
A1758a	0.28	28				2.53×10^{-3}	7.1	5, 11		45
A1914	0.17	30	1.09	50-100	2.0	2.16×10^{-2}	10.5	9, 13	44	46
A2163	0.20	104	1.70	20-80	1.5	3.23×10^{-2}	13.3	14, 15	42	46
A2219	0.23	40				9.84×10^{-3}	8.7	9, 18		45
A2255	0.08	79	2.73	20-80	2.0	1.39×10^{-2}	6.9	19, 20	43	46
A2256	0.06	116	2.41	50-100	2.0	4.32×10^{-2}	7.5	21, 22, 23	44	46
A2319	0.06	198	0.67	50-100	2.0	9.81×10^{-2}	9.2	24, 25	40	46
A2744	0.31	38	0.40	0.6-7	1.7	4.40×10^{-3}	7.2	18, 26	39	45
A3562	0.05	50	5.52	20-80	2.0	7.67×10^{-3}	5.2	27, 28	43	46
CL0217+70 ^{a,b}	0.07	78				5.70×10^{-3}	3.6	29		29
MACSJ0717.5+3745	0.55	12				9.12×10^{-3}	11.6	30, 31		47
MACSJ1752.0+4440 ^{a,c}	0.37	23				1.93×10^{-3}	6.7	32, 33		32, 33
PLCK G171.9-40.7 ^a	0.27	8				4.48×10^{-3}	10.7	34		34
RXCJ1514.9-1523 ^{a,b}	0.22	40				3.44×10^{-3}	6.4	35		48
RXCJ2003.5-2323 ^{a,b}	0.32	20				2.06×10^{-3}	6.8	36, 37		48

Notes. We estimate the size (in arcmin²) of the halo in the sky in order to scale the ASTRO-H sensitivity correspondingly. In case of approximately spherical sources, this is conservatively estimated to be $\pi D_{LLS}/4$, with D_{LLS} the largest linear size. For elongated sources, this is approximated by a box (or ellipse) whose longest extent (or major axis) is D_{LLS} . $F_{X, UL}$ is the current upper limit on the non-thermal hard X-ray flux in units of 10^{-12} erg cm⁻² s⁻¹, with $\Delta E_{X, UL}$ the corresponding energy band. Γ is the literature spectral index used to derive $F_{X, UL}$ and then used to calculate the flux density for our analysis. The flux is defined as $f_x = k_x \int_{\nu_{min}}^{\nu_{max}} \nu_x^{-\Gamma} d\nu_x$, where k_x is a constant. The flux density is $s_x(\nu) = k_x \nu_x^{-\Gamma}$, with Γ the spectral index of the IC component. The ICM temperature, kT , in keV is also shown. The three columns of references are for the radio data, the non-thermal hard X-ray upper limit and for the input parameters of the APEC model, respectively. ^(a) Gas density from Zandanel et al. (2014). ^(b) Temperature from $T - M_{500}$ relation of Mantz et al. (2010). ^(c) M_{500} from $L_{X, ROSAT} - M_{500}$ relation of Mantz et al. (2010).

References. (1) Liang et al. (2000); (2) Shimwell et al. (2014); (3) Vacca et al. (2014); (4) Brunetti et al. (2008); (5) Giovannini et al. (2009); (6) Macario et al. (2013); (7) Feretti et al. (2004); (8) van Weeren et al. (2011a); (9) Bacchi et al. (2003); (10) Kassim et al. (2001); (11) Giacintucci (2011); (12) Thierbach et al. (2003); (13) Komissarov & Gubanov (1994); (14) Feretti et al. (2001); (15) Feretti et al. (2004); (16) Kempner & Sarazin (2001); (17) Giovannini & Feretti (2000); (18) Orru et al. (2007); (19) Feretti et al. (1997); (20) Govoni et al. (2005); (21) Clarke & Ensslin (2006); (22) Brentjens (2008); (23) van Weeren et al. (2012); (24) Feretti et al. (1997); (25) Storm et al. (2015); (26) Govoni et al. (2001); (27) Venturi et al. (2003); (28) Giacintucci et al. (2005); (29) Brown et al. (2011); (30) Bonafede et al. (2009a); (31) Pandey-Pommier et al. (2013); (32) Bonafede et al. (2012); (33) van Weeren et al. (2012a); (34) Giacintucci et al. (2013); (35) Giacintucci et al. (2011); (36) Venturi et al. (2009); (37) Giacintucci et al. (2009); (38) Wik et al. (2014); (39) Million & Allen (2009); (40) Ajello et al. (2009); (41) Wik et al. (2011); (42) Ota et al. (2014); (43) Wik et al. (2012); (44) Ajello et al. (2010); (45) Fukazawa et al. (2004); (46) Chen et al. (2007); Pinzke et al. (2011); (47) Ma et al. (2008); (48) Piffaretti et al. (2011).

strength. The average energy of an IC up-scattered photon is $\langle \epsilon_1 \rangle = (4/3) \gamma^2 \langle \epsilon \rangle \approx 8.6 \times 10^{-7} \gamma^2$ keV, where we assumed the incoming CMB photon to be at redshift 0. We can use the monochromatic approximation for the synchrotron emission, which yields $(\nu/1 \text{ GHz}) = 1.05 \times 10^{-9} \gamma^2 (B/1 \mu\text{G})$. In case of $B = 1 \mu\text{G}$, synchrotron radiation at ~ 100 (20) MHz is produced by the electrons that generate IC emission at 80 (20) keV, while for $B = 5 \mu\text{G}$ one finds that ~ 480 (120) MHz radio waves correspond to 80 (20) keV X-rays. Therefore, low-frequency radio observations are crucial in order to precisely predict HXR IC emission, as will be discussed in Sect. 8, and to eventually clarify whether our assumption of Sect. 3 regarding the electron distribution holds down to low energies.

5. Background emission

In this section, we discuss the main background emission for IC searches in clusters. These are the thermal ICM bremsstrahlung and the cosmic X-ray background (CXB) emission. In Section 7, we will also introduce the instrumental background.

5.1. Thermal bremsstrahlung from ICM

In order to model the thermal bremsstrahlung emission from the ICM, we use the APEC code (Smith et al., 2001) as provided in the XSPEC software (Arnaud, 1996). The input parameters are the ICM temperature (taken, for most nearby clusters, from Chen et al., 2007), the redshift z , the metal abundance, which we fix to 0.3 times the solar abundance for simplicity (e.g., Böhringer

Table 2. Radio relic sample

Cluster	Source	z	Size	$F_{X, UL}$	$\Delta E_{X, UL}$	Γ	APEC Normalisation	kT	Ref. 1	Ref. 2	Ref. 3
Toothbrush ^{a,c}		0.23	18				6.4×10^{-4}	7.8	1		49
A0013		0.09	5				3.0×10^{-3}	6.0	2		50
A0085		0.06	26	2.5	50-100	2.0	5.1×10^{-3}	6.1	2	43	51
A0521		0.25	9				5.9×10^{-5}	4.9	3		52
A0610 ^{a,b,e}		0.10	8				1.3×10^{-4}	2.4	4		54
AS753 ^a		0.01	318				4.2×10^{-4}	2.5	5		5
A0754		0.05	100				9.0×10^{-3}	9.0	6, 7		6
A0781 ^{a,b}		0.30	6				3.4×10^{-5}	7.6	8		55
A1240	N	0.16	12				3.7×10^{-6}	6.0	9		56
	S	0.16	24				1.5×10^{-6}		9		
A1300		0.31	6				1.8×10^{-5}	6.3	10, 11		52
A1367		0.02	52	8.2	20-80	2.0	2.7×10^{-4}	3.6	12	63	51
A1612 ^{a,b}		0.18	8				3.3×10^{-6}	4.9	13		57
Coma		0.02	400	0.3	0.3-10	2.2	8.5×10^{-4}	8.4	14	45	51
A1664		0.13	51				6.0×10^{-4}	6.8	8		27
A2048 ^{a,b,d}		0.10	7				4.0×10^{-4}	4.2	15		58
A2061		0.08	24				6.6×10^{-4}	4.5	13, 16		59
A2063		0.03	3	7.6	20-80	2.0	3.6×10^{-3}	3.7	17	44	51
A2163		0.20	5				1.6×10^{-5}	13.3	18, 19		51
A2255		0.08	32				3.2×10^{-4}	6.9	20		51
A2256		0.06	152				2.3×10^{-2}	7.5	21, 22, 23		51
A2345 ^{a,b}	E	0.18	38				2.6×10^{-4}	6.5	24		53
	W		35				8.5×10^{-4}		24		
A2433 ^{a,b,e}		0.11	11				2.7×10^{-5}	1.8	25		60
A2744		0.31	19	0.4	0.6-7	1.7	6.6×10^{-5}	7.2	26, 27	46	52
A3376	E	0.05	324	3.5	8-Apr	2.0	5.4×10^{-3}	4.3	28	47	51
	W		122	1.1	8-Apr	2.0	3.1×10^{-5}		28	47	
A3411 ^a		0.17	62				3.2×10^{-3}	6.4	29		29
A3667	NW	0.06	250	0.6	Oct-40	1.8	6.6×10^{-4}	7.0	30, 31, 32	48	51
	SE		175				1.9×10^{-3}		31, 32		
A4038		0.03	12	7.4	20-80	2.0	2.8×10^{-4}	3.2	2, 8	44	51
El-Gordo ^a	E	0.87	3				2.7×10^{-2}	14.5	33		61
	NW		3				2.7×10^{-2}		33		
	SE		3				2.7×10^{-2}		33		
Sausage ^{a,b,c}		0.19	18				1.1×10^{-5}	5.6	34		57
MACSJ1149.5+2223 ^a	E	0.54	2				2.5×10^{-7}	14.5	35		35
	W		2				4.8×10^{-7}		35		
MACSJ1752.0+4440 ^{a,c}	NE	0.37	8				6.3×10^{-6}	6.7	35, 36		35, 36
	SW		3				1.2×10^{-5}		35, 36		
PLCK G287.0+32.9 ^{a,c}	N	0.39	7				7.4×10^{-5}	12.9	37		57
	S	0.39	6				5.2×10^{-7}	12.9	37		
RXCJ1314.4-2515	E	0.25	8				3.5×10^{-6}	7.2	38, 39		57
	W		15				2.3×10^{-4}		38, 39		
ZwCl0008.8-5215 ^{a,b}	E	0.10	36				1.3×10^{-4}	5.0	40		53
ZwCl2341.1+0000 ^a	N	0.27	4				8.7×10^{-5}	9.3	41, 42		62
	S		20				1.9×10^{-4}		41, 42		

Notes. Columns are as in Table 1, with the addition of the second column which indicates the specific relic to which we are referring to. ^(a) Gas density from Zandanel et al. (2014). ^(b) Temperature from $T - M_{500}$ relation of Mantz et al. (2010). ^(c) M_{500} from $L_{X,ROSAT} - M_{500}$ relation of Mantz et al. (2010). ^(d) M_{500} from $L_{X,bolometric} - M_{500}$ of Mantz et al. (2010). ^(e) M_{500} scaled from M_{200} .

References. (1) van Weeren et al. (2012b); (2) Slee et al. (2001); (3) Macario et al. (2013); (4) Giovannini & Feretti (2000); (5) Subrahmanyan et al. (2003); (6) Bacchi et al. (2003); (7) Kassim et al. (2001); (8) Kale & Dwarakanath (2012); (9) Bonafede et al. (2009b); (10) Reid et al. (1999); (11) Giacintucci (2011); (12) Gavazzi & Trinchieri (1983); (13) van Weeren et al. (2011a); (14) Thierbach et al. (2003); (15) van Weeren et al. (2011c); (16) Kempner & Sarazin (2001); (17) Komissarov & Gubanov (1994) (18) Feretti et al. (2001); (19) Feretti et al. (2004); (20) Feretti et al. (1997); (21) Clarke & Ensslin (2006); (22) Brentjens (2008); (23) van Weeren et al. (2012); (24) Bonafede et al. (2009b); (25) Cohen & Clarke (2011); (26) Orru et al. (2007); (27) Govoni et al. (2001); (28) Kale et al. (2012); (29) van Weeren et al. (2013); (30) Rottgering et al. (1997); (31) Hindson et al. (2014); (32) Johnston-Hollitt (2004); (33) Lindner et al. (2014); (34) Stroe et al. (2014); (35) Bonafede et al. (2012); (36) van Weeren et al. (2012a); (37) Bagchi et al. (2011); (38) Feretti et al. (2005); (39) Venturi et al. (2007); (40) van Weeren et al. (2011b); (41) van Weeren et al. (2009); (42) Bagchi et al. (2002); (43) Ajello et al. (2010); (44) Wik et al. (2012); (45) Feretti & Neumann (2006); (46) Million & Allen (2009); (47) Kawano et al. (2009); (48) Nakazawa et al. (2009); (49) Ogrea et al. (2013); (50) Juett et al. (2008); (51) Chen et al. (2007); (52) Pinzke et al. (2011); (53) Fukazawa et al. (2004) (54) Planck Collaboration et al. (2014); (55) Yoon et al. (2008); (56) Sehgal et al. (2008); (57) Barrena et al. (2009); (58) Cavagnolo et al. (2009); (59) Piffaretti et al. (2011); (60) Shen et al. (2008); (61) Marini et al. (2004); (62) Popesso et al. (2007); (63) Menanteau et al. (2012); (64) Boschini et al. (2013); (65) Henriksen & Mushotzky (2001).

& Werner, 2010), and the normalisation. The latter contains information about the ICM gas distribution that, for our purposes, can be approximated with a beta model (e.g., Cavaliere & Fusco-Femiano, 1976),

$$n_e(r) = \left[\sum_i n_{0,i}^2 \left(1 + \frac{r^2}{r_{c,i}^2} \right)^{-3\beta_i} \right]^{1/2}, \quad (4)$$

where n_0 is the central ICM electron density, and r_c is the core radius. Most clusters are well described by a single beta model ($i = 1$), whereas others are better described by a double beta model ($i = 1, 2$). The values of n_0 , r_c and β are derived from X-ray observations. For most nearby clusters, these values are taken from Pinzke et al. (2011).

In the few cases where we cannot find a gas density model in the literature, we adopt the phenomenological ICM model of Zandanel et al. (2014) which provides a gas density once the mass M_{500} of the cluster is known. In the few cases where no mass estimate is present in the literature, we adopt the X-ray luminosity-mass relation from Mantz et al. (2010). If there is no ICM temperature available in the literature, we also use the mass-temperature relation of Mantz et al. (2010). Obviously, such approximations are a source of uncertainty when used in particular cases and, therefore, the modelling of those clusters should be taken with caution. This is also true in general for relics where the gas density profiles have been inferred from X-ray observations of the clusters' center.

In the case of radio halos, the bremsstrahlung luminosity, L_B , is obtained by integrating over the full extent of the halo, where we approximate the halo to be spherical and use the largest linear size as given in Feretti et al. (2012) as halo diameter. In the case of radio relics in the outskirts of clusters, we only integrate over the relic region as:

$$L_B \sim (1 - \cos \phi) \int_{R_{cc}-0.5R_w}^{R_{cc}+0.5R_w} n_e(r)^2 r^2 dr, \quad (5)$$

where R_{cc} is the distance to the cluster center, R_w is the approximate width of the relic, and $\phi = \tan^{-1}[0.5R_l/(R_{cc} - 0.5R_w)]$ with R_l the largest linear size of the relic (see Fig. 1). For relics that are classified as roundish by Feretti et al. (2012), we use $R_w = R_l$.

The parameters that enter the APEC model are shown in Tables 1 and 2 for all the clusters in our sample.

5.2. Cosmic X-ray background

The CXB (e.g., Gilli et al., 2007) is another important background for the case of radio relics in the outskirts of clusters, where it often dominates over the thermal ICM emission. We assume the CXB to be isotropic across the sky and model it in the 0.5 – 100 keV regime as follows (Gruber, 1992; Comastri et al., 1995):

$$13.6 E^{-1} \text{ for } 0.5 \leq E < 2 \text{ keV},$$

$$7.877 E^{-0.29} e^{-E/(41.13 \text{ keV})} \text{ for } 2 \leq E < 60 \text{ keV},$$

$$1652 E^{-2} + 1.754 E^{-0.7} \text{ for } 60 \leq E \leq 100 \text{ keV},$$

in units of $\text{keV cm}^{-2} \text{ s}^{-1} \text{ sr}^{-1} \text{ keV}^{-1}$ and with E the photon energy in units of keV. Note that below 0.5 keV the galactic emission becomes an important source of background, but these low energies are not considered in this work.

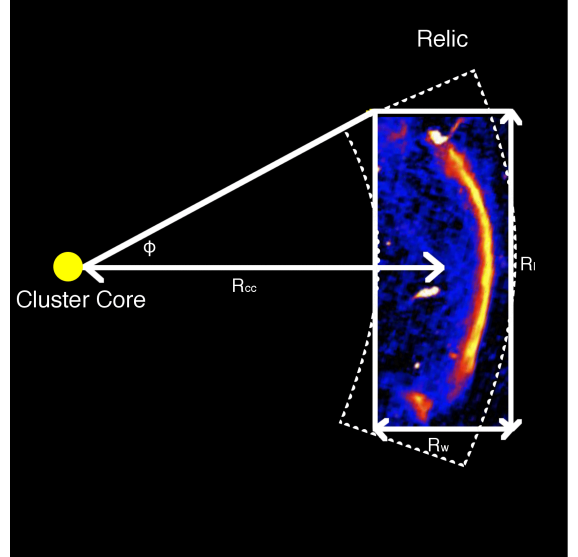


Fig. 1. The geometry used in determining the normalisation for the APEC modelling of the radio relic regions (Eq. 5). R_{cc} corresponds to the distance between the relic and the cluster center as projected on the sky. R_l is the relic largest linear size and R_w is the relic width. For relics that are classified as roundish by Feretti et al. (2012) we use $R_w = R_l$. ϕ is given by $\tan^{-1}\left(\frac{0.5R_l}{R_{cc}-0.5R_w}\right)$. In result, the dashed curve is the solid angle over which we integrate. The relic image, corresponding to the so-called Sausage, is adapted from Röttgering et al. (2013).

6. The ASTRO-H and NuSTAR satellites

In this section, we describe the characteristics of ASTRO-H that are relevant for this work. While we provide detailed predictions for the IC-emission detection by ASTRO-H, we also discuss in the same context the recently launched NuSTAR satellite.

6.1. ASTRO-H

ASTRO-H is a next generation X-ray satellite that is scheduled for launch in 2015 (Takahashi et al., 2012, 2014). The instruments that are of interest for our purposes are the Hard X-ray Imager (HXI) and the Soft X-ray Imager (SXI). In Table 3, we summarise the main characteristics of these instruments.

Table 3. Properties of the SXI and HXI detectors that will be on-board of ASTRO-H.

	SXI	HXI
Energy range [keV]	0.4–12.0	5–80
Angular resolution [arcmin]	1.3	1.7
Field of view (FoV) [arcmin ²]	38 × 38	9 × 9
Energy resolution [eV]	150 @6 keV	< 2000 @60 keV
Effective area [cm ²]	360 @6 keV	300 @30 keV

Notes. Values adopted from the ASTRO-H Quick Reference (<http://astro-h.isas.jaxa.jp/ahqr.pdf>).

To estimate the detectability of the non-thermal X-ray component in galaxy clusters, we make use of the sensitivity curves as published by the ASTRO-H collaboration for both point and extended sources (ASTRO-H Quick Reference,³ Takahashi

³ <http://astro-h.isas.jaxa.jp/ahqr.pdf>

et al., 2010, 2012). We adopt the sensitivity curve for 1 Ms of observation, and scale it to other observation times as $\sqrt{\text{time}}$. Note that the above mentioned ASTRO-H sensitivity curves are 3σ sensitivities, and that the sensitivity curve for extended sources assumes a uniform source of 1 deg^2 .

We assume, for simplicity, that halos and relics are uniform sources. In order to scale the sensitivity to the size, $\Omega \text{ arcmin}^2$, of a given object, we proceed as follows. For sources that are smaller than the HXI field of view, we scale the point-source sensitivity as $\sqrt{\Omega/2} \text{ arcmin}^2$, where 2 arcmin^2 is roughly the pixel size. For sources that are larger, we apply a linear scaling to the 1 deg^2 diffuse source sensitivity as $\Omega/3600 \text{ arcmin}^2$ (Hiroki Akamatsu, Madoka Kawaharada, private communication).

6.2. NuSTAR

The NuSTAR satellite was launched on June 13, 2012. Its performances in HXR should be comparable with ASTRO-H (Harrison et al., 2013), with the exception that ASTRO-H will be equipped with a pre-collimator designed to mitigate stray light (Mori et al., 2012).

Recently, Wik et al. (2014) pointed out that a possible IC signal has to be extracted from both the thermal and instrumental background, with the former dominating at low and the latter at high energies. In fact, the instrumental background is likely to dominate the count rate in the HXR. Since the instrumental background is modelled by a power-law, any claim of IC detection is extremely sensitive to the applied model. While the HXI detector onboard ASTRO-H will not improve much upon NuSTAR - in fact, our predictions are approximately valid in both cases - the presence of the SXI detector will greatly improve the modelling of the thermal component in clusters over the NuSTAR results.

7. Multi-band modelling and HXR detectability

For any given object in Tables 1 and 2, we proceed as follows. If there exist an upper limit on the non-thermal hard X-ray flux $F_{X,UL}$, we calculate the corresponding lower limit on the volume-average magnetic field B_V . First, we fix K_0 by fitting the IC spectrum of Eq. 3 to $F_{X,UL}$. Next, we fit the synchrotron emission of Eq. 2 to the radio data⁴, with B_V as free parameter. Depending on whether spectral steepening at low and/or high frequencies is observed, γ_{\min} and/or γ_{\max} are also determined from the data (see Sect. 3). The spectral index α is taken from the literature, unless it returns a poor fit, in which case we determine a new spectral index. The resulting broadband spectrum provides a lower limit on the magnetic field.

We then compare the background spectra (thermal bremsstrahlung and the CXB) to the properly scaled ASTRO-H sensitivity. We use the intersection between the ASTRO-H sensitivity curve and the dominant background component, either thermal ICM or CXB, to fix a new normalisation of the electron distribution K_0 using Eq. 3. This represents the lower limit on the normalisation detectable by ASTRO-H. If no upper limit on the hard X-ray flux, $F_{X,UL}$, exist for a given object, we start from this step. Finally, we fit again the synchrotron emission of Eq. 2 to the radio data. The resulting magnetic field value is a cap on the volume-average magnetic

⁴ Note that we neglect the possible effect at high frequencies of thermal Sunyaev-Zeldovich (SZ) decrement (e.g., EnBlin, 2002) that, however, should have a small impact (e.g., Brunetti et al., 2013). Anyhow, ignoring the SZ decrement implies more conservative results.

field below which HXR IC emission would be detectable by ASTRO-H, and we call it B_{dt} . To be clearer, HXR IC emission would be detectable by ASTRO-H if the cluster's magnetic field is lower or equal to B_{dt} , always meaning a volume-average. We underline that this simple approach is meant to be just a first-order approximation to what can really be achieved. In fact, e.g., the CXB background is well known and can be easily subtracted. We provide the result in such a case, along with the rest, in Tables 4 and 5.

The above approach leads to a rough estimate which we complement with one based on the total number of counts in the 20 – 80 keV band as follows. We require the signal-to-noise ratio $s/n = N_S / \sqrt{N_B + N_S} \geq 5$, where N_S is the total number of source counts and $\sqrt{N_B + N_S}$ is the corresponding noise, with $N_B = N_{ICM} + N_{CXB} + N_{instr}$ including all background counts (ICM, CXB and instrumental).

We approximate the instrumental background by a power-law corresponding to $6 \times 10^{-3} \text{ counts/s/keV/FoV}$ at 10 keV and $2 \times 10^{-4} \text{ counts/s/keV/FoV}$ at 50 keV, values adopted from the ASTRO-H Quick Reference (table 2). For our purpose, a simple power-law approximation of the instrumental noise suffices, since uncertainties will be dominated by the modelling of the thermal and IC emission.⁵ We convert the thermal bremsstrahlung and CXB fluxes into count rates by multiplying by the HXI effective area taken from the ASTRO-H Quick Reference (figure 1). N_S is then related to the HXR flux density, $S_x(E) = k_x E^{-\alpha}$, through

$$N_S = T_{\text{obs}} \int_{20 \text{ keV}}^{80 \text{ keV}} \frac{S_x(E) A_{\text{eff}}(E)}{E} dE, \quad (7)$$

where T_{obs} is the observation time and $A_{\text{eff}}(E)$ is the effective area. Using the N_S for which $s/n \geq 5$, we solve for k_x and, finally, calculate the corresponding flux as $F_x = k_x \int_{20 \text{ keV}}^{80 \text{ keV}} E^{-\alpha} dE$. The spectral index used here is the same as above. This flux is then converted into a magnetic field, $B_{dt}^{s/n}$, using

$$\frac{F_x \nu_r^{-\alpha}}{s_r \int_{\nu_{\min}}^{\nu_{\max}} \nu_x^{-\alpha} d\nu_x} = \frac{2.46 \times 10^{-19} T_{\text{CMB}}^3 b(p) \left(\frac{4.96 \times 10^3 T_{\text{CMB}}}{B_{dt}^{s/n}} \right)^\alpha}{B_{dt}^{s/n} a(p)}, \quad (8)$$

where $T_{\text{CMB}} = T_0(1+z)$ is the CMB temperature, F_x is the X-ray flux, s_r is the radio flux density at ν_r , $p = 2\alpha + 1$, and

$$a(p) = \frac{2^{(p-1)/2} \sqrt{3} \Gamma\left(\frac{3p-1}{12}\right) \Gamma\left(\frac{3p+19}{12}\right) \Gamma\left(\frac{p+7}{4}\right)}{16\pi^{1/2} \Gamma\left(\frac{p+9}{4}\right)}, \quad (9a)$$

$$b(p) = 2^{p+3} \frac{(p^2 + 4p + 11) \Gamma\left(\frac{p+5}{2}\right) \zeta\left(\frac{p+5}{2}\right)}{(p+3)^2 (p+1)(p+5)}, \quad (9b)$$

Here Γ and ζ are the gamma and Riemann zeta functions, respectively (Pacholczyk, 1970; Blumenthal & Gould, 1970; Sarazin, 1988; Longair, 2011).⁶ In this approach, for objects whose size in the sky ($\Omega \text{ arcmin}^2$) is larger than the HXI FoV ($9 \times 9 \text{ arcmin}^2$),

⁵ Additionally, comparing our power-law estimate to the ASTRO-H response files (<http://astro-h.isas.jaxa.jp/researchers/sim/response.html>) in the 20 – 80 keV band shows that we overestimate the predicted instrumental background by just a few percent.

⁶ Note that the arguments of the gamma function (Γ) are slightly different with respect to the values when a coherent magnetic field is assumed.

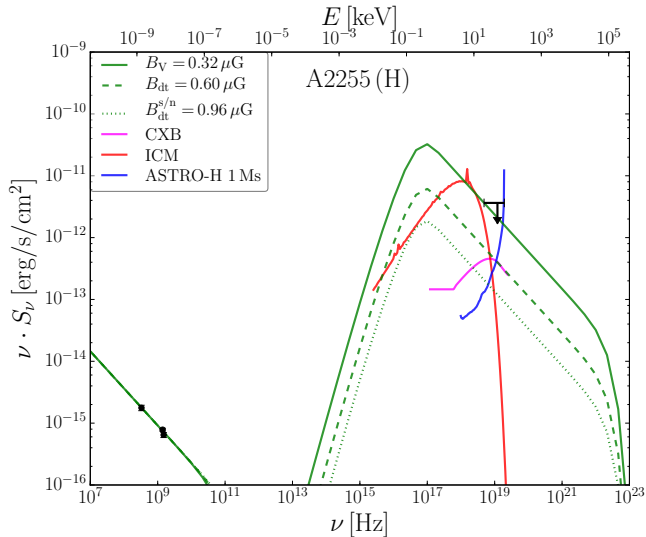


Fig. 2. Synchrotron and IC modelling of the radio halo (H) in A2255. The black points and arrow are the currently available radio data and HXR upper-limit, respectively, from Table 1. We show the thermal ICM and CXB emissions, together with the ASTRO-H HXI sensitivity for 1 Ms of observations scaled to the halo angular size. The green lines show the models for the current volume-average lower limit B_V (solid), and for B_{dt} (dashed) and $B_{dt}^{s/n}$ (dotted) for 1 Ms of observations.

the radio flux density s_r is roughly scaled down as $9 \times 9/\Omega$. This implies slightly conservative results as halos and relics are not uniform sources. Eventually, the resulting magnetic field value, $B_{dt}^{s/n}$, is again a cap on the volume-average magnetic field below which HXR IC emission is detectable by ASTRO-H.

The analysis based on the signal-to-noise ratio is done assuming a straight power-law in the 20–80 keV energy band. That is, we ignore any possible cutoff effect in that range, otherwise Eq. 8 would not be valid anymore. In most cases, the cutoffs are at much lower and higher energies. However, e.g., for A0085 and A1914 (see Fig. 3), and for A2063 and A0013 (see Appendix A for the corresponding figures), this method could give slightly optimistic results.

Note also that in some cases (only radio relics, see Appendix A for the figures), the CXB dominates over the thermal ICM emission, and the intersection point between the ASTRO-H sensitivity and the CXB emission is at an energy lower than the rise in the CXB spectrum. The corresponding results for B_{dt} should be taken with caution and, in fact, in these cases, the signal-to-noise approach gives more conservative results. We underline again that our simple approach is meant to be only a first-approximation, and that, in the following, we base all our conclusions only on the more robust signal-to-noise approach. Nevertheless, we also note that the two approaches turn out to give similar results.

We eventually decided to exclude the A2218 halo and the ZwCl0008.8-5215 western relic from the final modelling. This is due to their low radio flux, and to the apparent presence of a quite high γ_{min} , or break in the radio spectra, that would render rather impossible the IC search in these objects.

We show an example of synchrotron and IC modelling in Fig. 2 for the case of the radio halo hosted by A2255, and we present and discuss all results in the next sections.

8. Results

The results of our analysis are given in Tables 4 and 5 for radio halos and relics, respectively. The third column contains the current lower limit on the magnetic field for objects where an HXR flux upper limit is available in literature. Note that our lower limits on the magnetic field are slightly higher than those in the original works from which the HXR upper limits fluxes are taken because of our assumption on the magnetic field distribution (see Sect. 4). The sixth column contains B_{dt} , corresponding to the cap value of the volume-averaged magnetic field up to which ASTRO-H can still detect non-thermal IC for 1 Ms of observation time. The eighth column shows an optimistic value for the detection sensitivity on the volume-average magnetic field, B_{dt}^{opt} , obtained assuming that the CXB can be perfectly subtracted and, therefore, considering always the intersection of the ASTRO-H sensitivity curve with the thermal ICM emission as estimation point for B_{dt}^{opt} (see Sect. 7 for details).

In Tables 6 and 7, we show the estimate of the ASTRO-H detection sensitivity of the volume-average magnetic field, $B_{dt}^{s/n}$, obtained with the signal-to-noise approach in the 20–80 keV band, for halos and relics, respectively. We show the results for 100 ks, 500 ks and 1 Ms of observation time.

Comparing the results in Tables 4–7, it is clear that the former results based on the intersection point between the background emission and the ASTRO-H sensitivity are more pessimistic. In particular, for sources larger than the HXI FoV (e.g., the halos of Coma and A2319, and the relics of Coma and A3667), our initial analysis shows little room for improvement on the current constraints while the signal-to-noise analysis shows differently. The simplified assumption of a uniform source in our initial analysis is the most obvious reason for the pessimistic perspective for sources that cover a large area on the sky. This is also the origin for the B_{dt} values of the Coma and A2319 radio halos and the Coma and A3667-NW relic to be at the same level of current upper limits. Additionally, as a general remark, assuming that the IC emission is detectable only at energies where it dominates over the background is a conservative approach, giving that backgrounds are known and can be modelled in detail in a real analysis. Indeed, as already stressed earlier, this simple method is meant to be just a first-order approximation, and we take our signal-to-noise approach as reference when drawing conclusions.

Note that the soft X-ray (SXR) and extreme ultra-violet (EUV) bands could also be promising for the detection of IC emission, since the flux would be much higher at those lower frequencies (e.g., Sarazin & Lieu, 1997). However, this is advantageous only if the background can be well constrained, and crucially depends on the low energy cutoff of the relativistic electron population, γ_{min} , which is, in most cases, unconstrained by current radio data. Indeed, assuming an electron spectrum cutoff of $\gamma_{min} \sim 10^2$, as discussed in Section 3, implies IC spectra peaking in the EUV band and often dominating over the X-ray background in SXRs, in particular in case of very steep radio spectra. However, such steep spectra down to very low frequencies seem unlikely. The radio spectrum depends on acceleration history of relativistic electrons and, e.g., steady state injection models feature a spectral break and would imply a low-frequency flattening (e.g., Sarazin, 1999). In the near future, low-frequency observations with LOFAR (Röttgering et al., 2012) will provide crucial information and certainly shed more light on the spectrum of cosmic-ray electrons in clusters. This will be vital in order to assess the possible IC contribution in the SXR and EUV regimes.

Table 4. Results for halos

Cluster	α	Current Limits	ASTRO-H 1 Ms	$B_{\text{dt}}^{\text{opt}}$	E	$S_x \times E$
		B_V [μG]	B_{dt} [μG]	[μG]		
Bullet	1.50	0.38	1.00	1.00	45	0.20
A0520	1.12		0.37	0.57	33 (16)	0.14 (0.06)
A0521	1.81		0.80	1.16	31 (18)	0.11 (0.06)
A0665	1.04	0.11	0.28	0.41	46 (29)	0.42 (0.20)
A0697	1.52		0.33	0.33	53	0.29
A0754	1.10	$0.09\gamma_{\text{max}}=6.0\times 10^4$	$0.45\gamma_{\text{max}}=2.7\times 10^4$	0.45	52	0.47
A1300	1.76		1.02	1.27	30 (23)	0.10 (0.07)
Coma	1.16	$0.32\gamma_{\text{max}}=3.9\times 10^4$	$0.36\gamma_{\text{max}}=3.7\times 10^4$	0.36	48	3.67
A1758a	1.50		0.71	0.95	34	0.16
A1914	1.95	$0.59\gamma_{\text{min}}=2.3\times 10^3$	$1.12\gamma_{\text{min}}=1.7\times 10^3$	1.12	51	0.33
A2163	1.18	0.13	0.49	0.49	57	0.82
A2219	0.72		0.29	0.30	39 (37)	0.22 (0.21)
A2255	1.60	0.32	0.60	0.77	46 (34)	0.42 (0.27)
A2256	1.35	0.20	0.49	0.53	48	0.60
A2319	1.65	0.66	0.65	0.65	53	1.36
A2744	0.92	0.29	0.44	0.59	39 (26)	0.21 (0.12)
A3562	1.30	$0.10\gamma_{\text{max}}=6.8\times 10^4$	$0.37\gamma_{\text{max}}=3.5\times 10^4$	0.53	41 (27)	0.27 (0.14)
CL0217+70 ^a	1.20		0.36	0.69	46 (17)	0.41 (0.12)
MACSJ0717.5+3745	1.23		1.29	1.29	40	0.12
MACSJ1752.0+4440 ^a	1.60		0.97	1.37	32 (20)	0.13 (0.07)
PLCK G171.9-40.7 ^a	1.84		1.15	1.15	42	0.11
RXCJ1514.9-1523 ^a	1.60		0.52	0.76	39 (24)	0.22 (0.11)
RXCJ2003.5-2323 ^a	1.32		0.92	1.19	31 (22)	0.11 (0.07)

Notes. For each object, we show α and report the values of the current lower limit on the volume-average magnetic field, B_V , where available, and the detection sensitivity on the volume-average magnetic field, B_{dt} , for which IC emission would be detectable by ASTRO-H in 1 Ms. Additionally, $B_{\text{dt}}^{\text{opt}}$ is an optimistic estimate of the latter that corresponds to the intersection of the sensitivity curve and the thermal ICM emission, thus assuming the CXB is fully known and perfectly subtracted. The last two columns shows the energy where non-thermal X-rays start to dominate over the background for B_{dt} ($B_{\text{dt}}^{\text{opt}}$), and the corresponding non-thermal flux density in units of in 10^{-12} erg cm $^{-2}$ s $^{-1}$, respectively. In the cases where γ_{min} and/or γ_{max} are calculated from the radio data and differ from the standard values that we adopt (see Sect. 3), we show them explicitly. ^(a) Thermal ICM emission computed using the model by Zandanel et al. (2014) for the gas density.

8.1. Promising targets

In order to pinpoint the most promising targets for ASTRO-H HXR observations, we focus on magnetic field estimates (e.g., Govoni & Feretti, 2004). FR measurements range from $\sim \mu\text{G}$ for merging clusters up to $10 \mu\text{G}$ for cool-core clusters (Carilli & Taylor, 2002; Clarke, 2004; Vogt & EnBlin, 2005; Bonafede et al., 2010; Bonafede et al., 2013). Therefore, μG -level magnetic fields in clusters are nowadays widely acknowledged.

Analytical estimates can be obtained by the equipartition argument, i.e., minimising the total energy content, sum of the energies of the magnetic field and relativistic particles, of a radio source. While standard equipartition estimates, B_{eq} , are based on computing the synchrotron radio luminosity between two fixed frequencies, the so-called revised equipartition estimates, $B_{\text{eq}}^{\text{rev}}$, are based on integrating over the relativistic electron distribution (Brunetti et al., 1997; Beck & Krause, 2005). In Table 8, we summarise all the (revised) equipartition estimates that we could find in literature for the clusters in our sample.

We stress that the equipartition estimates compiled in Table 8 should be considered only as reference values for comparison purposes. Not only these suffer from several uncertainties such as, e.g., the ratio of electrons to protons in the source and the low-energy cutoff of the electron distribution which are, a priori, unknown (see Govoni & Feretti, 2004 for a discussion), but also one could question whether the equipartition assumption is motivated as the evolution of relativistic electrons and magnetic

fields in clusters may be decoupled given the short lifetime of the electrons compared to that of clusters. We also note that different authors often adopt different assumptions when applying the equipartition argument.

We consider a given halo or relic to be a promising candidate for ASTRO-H if its $B_{\text{dt}}^{\text{opt}}$ in 100 ks of observations is $\geq 1 \mu\text{G}$; while if smaller, we consider it promising if that value is comparable to, or higher than, the corresponding (revised) equipartition estimate (where available). The value of $1 \mu\text{G}$ is just a rough educated guess assuming as prototype magnetic field value that of the Coma cluster for which the volume-average is $\sim 2 \mu\text{G}$ (Bonafede et al., 2010; Bonafede et al., 2013). We summarise all objects that meet these criteria in Table 9.

There is a crucial point to be considered when looking at our summary list of promising targets in Table 9. That is the size in the sky of a given halo; this plays a crucial role for our predictions. Several objects in Table 9 have a size well below the ASTRO-H HXI FoV of $9 \times 9 = 81$ arcmin 2 . The smaller the size of a given object with respect to the FoV, the higher is the contamination given by the thermal ICM emission which obviously peaks in the centre of clusters. This is particularly important for radio relics in the cluster's outskirts which are the best targets for HXR IC detection, as clear from the results presented in the tables of this work. On the other hand, an object much larger than the ASTRO-H FoV will call for multiple pointings with the corresponding increase in observation time. ASTRO-H observa-

Table 5. Results for relics

Cluster	Source	α	Current Limits	ASTRO-H 1Ms	$B_{\text{dt}}^{\text{opt}}$ [μG]	E [keV]	$S_x \times E$
			B_V [μG]	B_{dt} [μG]			
Toothbrush ^a		1.10		1.65	2.13	31 (22)	0.11 (0.07)
A0013		2.30		1.98 _{$\gamma_{\text{min}}=2.6 \times 10^3$}	1.98	31 (31)	0.06 (0.06)
A0085		1.61	0.43 _{$\gamma_{\text{max}}=1.6 \times 10^4$ $\gamma_{\text{min}}=3.1 \times 10^3$}	1.79 _{$\gamma_{\text{max}}=7.7 \times 10^3$ $\gamma_{\text{min}}=1.5 \times 10^3$}	1.96	34 (31)	0.15 (0.13)
A0521		1.45		1.00	2.00	24 (6)	0.05 (0.02)
A0610 ^a		1.40		0.86	1.51	23 (8)	0.05 (0.02)
AS753 ^a		2.10		1.08 _{$\gamma_{\text{max}}=2.0 \times 10^4$}	4.82	49 (5)	1.75 (0.23)
A0754		1.10		0.28	0.32	48(40)	0.52(0.39)
A0781 ^a		1.23		1.06	1.76	17(5)	0.03(0.01)
A1240	N	0.86		0.16	0.28	28 (5)	0.07 (0.02)
	S	0.71		0.10	0.18	34 (5)	0.15 (0.03)
A1300		0.90		0.60	0.79	17	0.03
A1367		1.90	0.89	0.76	2.16	43 (10)	0.29 (0.05)
A1612 ^a		1.40		1.64	3.39	23 (5)	0.05 (0.02)
Coma		1.18	0.87	0.28	0.65	49 (13)	2.20 (0.46)
A1664		1.10		0.52	0.90	43 (18)	0.29 (0.10)
A2048 ^a		2.29		2.43	2.96	20 (15)	0.04 (0.03)
A2061		1.03		0.31	0.48	34 (16)	0.15 (0.06)
A2063		1.21	0.42 _{$\gamma_{\text{max}}=1.4 \times 10^4$}	5.51 _{$\gamma_{\text{max}}=4.0 \times 10^3$}	5.51	24	0.03
A2163		1.02		0.75	0.99	16	0.03
A2255		1.40		0.38	0.63	37 (17)	0.19 (0.08)
A2256		0.81		0.34	0.41	49 (39)	0.84 (0.57)
A2345 ^a	E	1.30		0.49	0.99	40 (14)	0.22 (0.06)
	W	1.56		0.73	1.20	39 (19)	0.20 (0.09)
A2433 ^a		1.74		1.38 _{$\gamma_{\text{max}}=9.3 \times 10^3$}	2.52	27 (5)	0.07 (0.02)
A2744		1.10	0.35	0.51	1.09	31 (6)	0.11 (0.03)
A3376	E	0.88	0.13 _{$\gamma_{\text{max}}=3.9 \times 10^4$}	0.30 _{$\gamma_{\text{max}}=2.5 \times 10^4$}	0.59	49 (16)	1.78 (0.45)
	W	1	0.26 _{$\gamma_{\text{max}}=3.0 \times 10^4$}	0.48 _{$\gamma_{\text{max}}=2.2 \times 10^4$}	1.32	49 (5)	0.67 (0.09)
A3411 ^a		1		0.38	0.59	45 (25)	0.34 (0.14)
A3667	NW	1.02	1.29	0.94	2.12	49 (12)	1.37 (0.27)
	SE	0.95		0.31	0.53	49 (21)	0.96 (0.32)
A4038		1.18	0.20 _{$\gamma_{\text{max}}=2.5 \times 10^4$}	1.88 _{$\gamma_{\text{max}}=8.2 \times 10^3$}	3.11	28 (11)	0.07 (0.03)
El-Gordo ^a	E	0.90		0.12	0.12	51	0.10
	NW	1.19		0.77	0.77	51	0.10
	SE	1.40		0.41	0.41	51	0.10
Sausage ^a		1.06		0.73 _{$\gamma_{\text{max}}=5.4 \times 10^4$}	1.62	31 (5)	0.11 (0.02)
MACSJ1149.5+2223 ^a	E	1.20		1.63	1.63	5	0.01
	W	0.80		0.66	0.66	5	0.01
MACSJ1752.0+4440 ^a	NE	1.16		1.69	3.17	23 (5)	0.05 (0.02)
	SW	1.10		2.45	2.45	5	0.01
PLCK G287.0+32.9 ^a	N	1.26		1.57	1.91	20 (14)	0.04 (0.03)
	S	1.54		2.26	4.14	17(5)	0.03(0.01)
RXCJ1314.4-2515	E	1.20		0.62	1.18	23 (5)	0.05 (0.02)
	W	1.40		0.83	1.28	30 (15)	0.09 (0.04)
ZwCl0008.8-5215 ^a	E	1.59		0.85	2.14	39 (9)	0.21 (0.04)
ZwCl2341.1+0000 ^a	N	0.49		0.13	0.13	16	0.02
	S	0.76		0.19	0.29	32 (16)	0.12 (0.05)

Notes. Columns are as in Table 4, with the addition of the second column which indicates the specific relic to which we are referring to. ^(a) Thermal ICM emission computed using the model by Zandanel et al. (2014) for the gas density. ^(b) No improvement upon current constraints are possible according to this analysis (see main text for details).

tion simulations of these objects, considering their morphology, is needed in order to give a definitive answer on which are the most promising targets.

Note that we include Coma in our list of promising targets mainly because it is one of the best studied clusters and its observation by ASTRO-H is desirable. In fact, Coma represents one of the best targets where to detect and map for the first time the bulk of the ICM turbulent velocities with the Soft X-ray Spectrometer

(SXS) on-board ASTRO-H (Kitayama et al., 2014). However, it does not represent the best hopes for the HXR IC detection.

In order to facilitate the interpretation of our results, we provide a simple, approximate, scaling of the ASTRO-H observation time with the magnetic field value $B_{\text{dt}}^{s/n}$ corresponding to the signal-to-noise approach. We note that the number of background counts scales linearly with time $N_B \propto T_{\text{obs}}$, and, under the assumption that $N_B \gg N_s$, one finds that the number

Table 6. S/N results for halo

Cluster	s_r	ν_r	ASTRO-H 100 ks		500 ks		1 Ms	
			$B_{dt}^{s/n}$	$F_{20-80\text{keV}}^a$	$B_{dt}^{s/n}$	$F_{20-80\text{keV}}^a$	$B_{dt}^{s/n}$	$F_{20-80\text{keV}}^a$
	[mJy]	[MHz]	[μG]		[μG]		[μG]	
Bullet	52	1340	0.84	0.42	1.18	0.18	1.37	0.13
A0520	85	325	0.26	0.40	0.39	0.17	0.46	0.12
A0521	328	153	0.61	0.28	0.83	0.12	0.94	0.08
A0665	197	327	0.25	0.72	0.38	0.31	0.45	0.22
A0697	135	153	0.25	0.85	0.35	0.37	0.40	0.26
A0754	86	1365	0.27	0.97	0.40	0.42	0.48	0.30
A1300	130	325	0.74	0.28	1.02	0.12	1.16	0.08
Coma*	640	1400	0.20	1.88	0.29	0.83	0.34	0.59
**	"	"	0.54	"	0.79	"	0.93	"
***	"	"	0.25	1.11	0.37	0.49	0.44	0.34
A1758	146	325	0.55	0.38	0.78	0.16	0.90	0.11
A1914	64	1465	1.18	0.53	1.57	0.23	1.77	0.16
A2163*	861	325	0.46	1.08	0.67	0.47	0.79	0.33
**	"	"	0.51	"	0.75	"	0.88	"
A2219	232	325	0.19	0.66	0.31	0.28	0.38	0.20
A2255	536	330	0.61	0.64	0.84	0.28	0.96	0.20
A2256*	6600	63	0.41	0.87	0.58	0.38	0.68	0.27
*	"	"	0.48	"	0.68	"	0.79	"
A2319*	1450	408	0.56	1.20	0.77	0.53	0.88	0.37
**	"	"	0.79	"	1.08	"	1.23	"
A2744	218	325	0.32	0.55	0.49	0.23	0.59	0.16
A3562	20	1400	0.26	0.55	0.38	0.24	0.44	0.17
CL0217+70 ^a	326	325	0.33	0.68	0.48	0.29	0.56	0.21
MACSJ0717.5+3745	493	235	0.91	0.37	1.35	0.15	1.58	0.11
MACSJ1752.0+4440 ^a	164	323	0.73	0.34	1.02	0.14	1.17	0.10
PLCK G171.9-40.7 ^a	483	235	0.98	0.26	1.33	0.11	1.52	0.08
RXCJ1514.9-1523 ^a	102	327	0.46	0.44	0.63	0.19	0.73	0.13
RXCJ2003.5-2323 ^a	360	240	0.64	0.35	0.93	0.15	1.09	0.10

Notes. For each halo, we show the radio data values s_r and ν_r used in Eq. 8 to calculate $B_{dt}^{s/n}$. We show the latter for 100 ks, 500 ks and 1 Ms of ASTRO-H observations, together with the corresponding flux in the 20 – 80 keV energy band in units of $10^{-12} \text{ erg cm}^{-2} \text{ s}^{-1}$. Within a few percent error the fluxes and magnetic fields scale with observation time according to Eq. 10. ^(*) In this cases, the source is larger than the HXI FoV of $9 \times 9 = 81 \text{ arcmin}^2$. In our work, for simplicity, we assumed a uniform surface brightness and, therefore, s_r was scaled by a factor $81/x$ where $x \text{ arcmin}^2$ is the size that a source covers in the sky (see Tables 1 and 2). Note that this estimate results in slightly conservative predictions since halos and relics are non-uniform sources. ^(**) This gives results assuming all radio emission is coming from an area equal to the HXI FoV and, therefore, s_r was not scaled. This can be considered an optimistic estimate for the detectable magnetic field. ^(***) Additional analysis for Coma. Since the Coma radio halo is extremely large in the sky, we estimated the thermal ICM emission only in the HXI FoV, integrating Eq. 4 out to $\sim 180 \text{ kpc}$, roughly corresponding to the HXI FoV, rather than over the full halo size. ^(a) Thermal ICM emission computed using the model by Zandanel et al. (2014) for the gas density.

of source counts necessary to reach a fixed signal-to-noise ratio scales as $N_S \sim \sqrt{T_{\text{obs}}}$. From Eq. 7, $F_x \propto N_S/T_{\text{obs}} \propto T_{\text{obs}}^{-1/2}$, and, eventually, from Eq. 8, we obtain that, for a given α ,

$$B_{dt}^{s/n} \propto T_{\text{obs}}^{\frac{1}{2(1+\alpha)}}. \quad (10)$$

Analogously, it can be shown that for a fixed observation time, i.e., fixed N_B , the detectable magnetic field depends on the signal-to-noise ratio as follows:

$$B_{dt}^{s/n} \propto (s/n)^{-\frac{1}{(1+\alpha)}}. \quad (11)$$

8.2. Comments on individual clusters

We report in the following some comments on the individual clusters in our final list of most promising objects - A0085, AS753, A3667, Bullet, A1914, A2255, A2319, and Coma - while we leave the rest for Appendix A. We show the corresponding synchrotron and IC modelling in Figs. 2, 3, and 4.

A0085. As can be seen from the top-left panel of Fig. 3, the radio relic of A0085 appears to have a low-energy cutoff in the radio spectrum. While this cutoff seems to not impact our conclusion for the ASTRO-H detectability, would the magnetic field be much larger than $B_{s/n}$, the low-energy turnover of the spectrum would move to higher energies and could impact the detectability estimates. Note also that the current HXR upper limit for this cluster (Ajello et al., 2010) refers to a much larger area than that of the relic. We remind the reader that the result of signal-to-noise approach should be taken with caution in this case as it assumes a straight power-law in the 20–80 keV range, while some spectral features could be expected.

AS753. The top-right panel of Figure 3 shows the synchrotron and IC modelling for the radio relic hosted by this cluster. There are two things that should be noted. First, the very steep radio spectrum which implies a very-large IC flux in SXR if we stick to the theoretically motivated $\gamma_{\text{min}} = 200$. For this reason, we show in the figure also the case with $\gamma_{\text{min}} = 1000$ and see that it does not impact much on our predictions for the

Table 7. S/N results for relics

Cluster	Source	s_r [mJy]	ν_r [MHz]	ASTRO-H 100 ks		500 ks		1 Ms	
				$B_{dt}^{s/n}$ [μ G]	$F_{20-80\text{keV}}^a$	$B_{dt}^{s/n}$ [μ G]	$F_{20-80\text{keV}}^a$	$B_{dt}^{s/n}$ [μ G]	$F_{20-80\text{keV}}^a$
Toothbrush ^a		7600	74	1.08	0.35	1.64	0.15	1.95	0.10
A0013		6000	80	1.10	0.14	1.45	0.06	1.63	0.04
A0085		8330	160	1.33	0.37	1.84	0.16	2.11	0.11
A0521		297	153	0.54	0.23	0.78	0.09	0.91	0.06
A0610 ^a		59	600	0.47	0.22	0.69	0.09	0.80	0.06
AS753 ^{*a}		460	1398	1.30	0.48	1.70	0.21	1.91	0.15
**		"	"	2.02	"	2.65	"	2.97	"
A0754 [*]		1450	74	0.22	0.80	0.33	0.35	0.39	0.24
**				0.25	"	0.37	"	0.44	"
A0781 ^a		93	325	0.48	0.21	0.72	0.09	0.85	0.06
A1240	N	21	325	0.09	0.32	0.14	0.13	0.17	0.09
	S	29	325	0.06	0.46	0.10	0.20	0.12	0.14
A1300		75	325	0.27	0.24	0.44	0.10	0.54	0.07
A1367		180	610	0.78	0.43	1.04	0.19	1.18	0.13
A1612 ^a		776	241	0.92	0.23	1.34	0.09	1.56	0.06
Coma [*]		3300	151	0.27	0.70	0.40	0.30	0.47	0.21
**		"	"	0.56	"	0.82	"	0.97	"
A1664		1250	150	0.45	0.58	0.67	0.25	0.79	0.17
A2048 ^a		559	325	1.41	0.15	1.86	0.06	2.08	0.04
A2061		104	327	0.20	0.42	0.31	0.18	0.36	0.12
A2063		13 200	178	2.25	0.17	3.46	0.07	4.12	0.05
A2163		82	325	0.30	0.22	0.48	0.09	0.57	0.06
A2255		103	330	0.22	0.42	0.31	0.18	0.36	0.13
A2256 ^{*a}		5600	63	0.26	0.94	0.41	0.41	0.50	0.29
**		"	"	0.37	"	0.58	"	0.71	"
A2345 ^a	E	188	325	0.41	0.47	0.59	0.20	0.68	0.14
	W	291	325	0.63	0.42	0.88	0.18	1.02	0.12
A2433 ^a		5310	74	0.90	0.23	1.24	0.10	1.42	0.07
A2744		98	325	0.33	0.37	0.50	0.15	0.59	0.11
A3376 [*]	E	122	1400	0.11	0.78	0.17	0.34	0.21	0.24
**		"	"	0.23	"	0.36	"	0.43	"
*	W	113	1400	0.24	0.74	0.36	0.32	0.43	0.23
**		"	"	0.29	"	0.44	"	0.53	"
A3411 ^a		2074	74	0.38	0.66	0.58	0.29	0.69	0.20
A3667 [*]	NW	81 000	86	1.12	0.74	1.70	0.32	2.02	0.23
**		"	"	1.95	"	2.94	"	3.51	"
*	SE	3200	120	0.30	0.77	0.46	0.33	0.55	0.23
**		"	"	0.44	"	0.68	"	0.81	"
A4038		380	606	0.67	0.29	1.00	0.12	1.18	0.08
Sausage ^a		96	1400	0.55	0.36	0.84	0.15	1.00	0.11
El-Gordo ^a	E	1	610	0.06	0.44	0.10	0.19	0.12	0.13
	NW	19	610	0.47	0.40	0.69	0.17	0.82	0.12
	SE	3	610	0.30	0.37	0.42	0.16	0.49	0.11
MACSJ1149.5+2223 ^a	E	23	323	0.40	0.14	0.63	0.05	0.75	0.04
	W	17	323	0.18	0.17	0.31	0.06	0.38	0.04
MACSJ1752.0+4440 ^a	NE	410	323	0.90	0.25	1.36	0.10	1.61	0.07
	SW	163	323	0.66	0.17	1.03	0.07	1.24	0.05
PLCK G287.0+32.9 ^a	N	550	150	0.77	0.23	1.14	0.09	1.35	0.06
	S	780	150	1.05	0.19	1.51	0.08	1.75	0.05
RXCJ1314.4-2515	E	28	610	0.33	0.24	0.49	0.10	0.58	0.07
	W	65	610	0.55	0.30	0.80	0.12	0.93	0.09
ZwCl0008.8-5215 ^a	E	820	241	0.72	0.41	1.00	0.18	1.15	0.12
ZwCl2341.1+0000 ^a	N	36	157	0.05	0.24	0.10	0.09	0.13	0.06
	S	70	157	0.10	0.42	0.17	0.18	0.21	0.12

Notes. Columns, and footnotes, are as in Table 6, with the addition of the second column which indicates the specific relic to which we are referring to.

HXR regime. Additionally, we must note that, lacking literature information on the gas density in this cluster, we used the phenomenological ICM model of Zandanel et al. (2014). This is,

obviously, a source of a uncertainty and likely resulted in an underestimation of the gas density at the relic location.

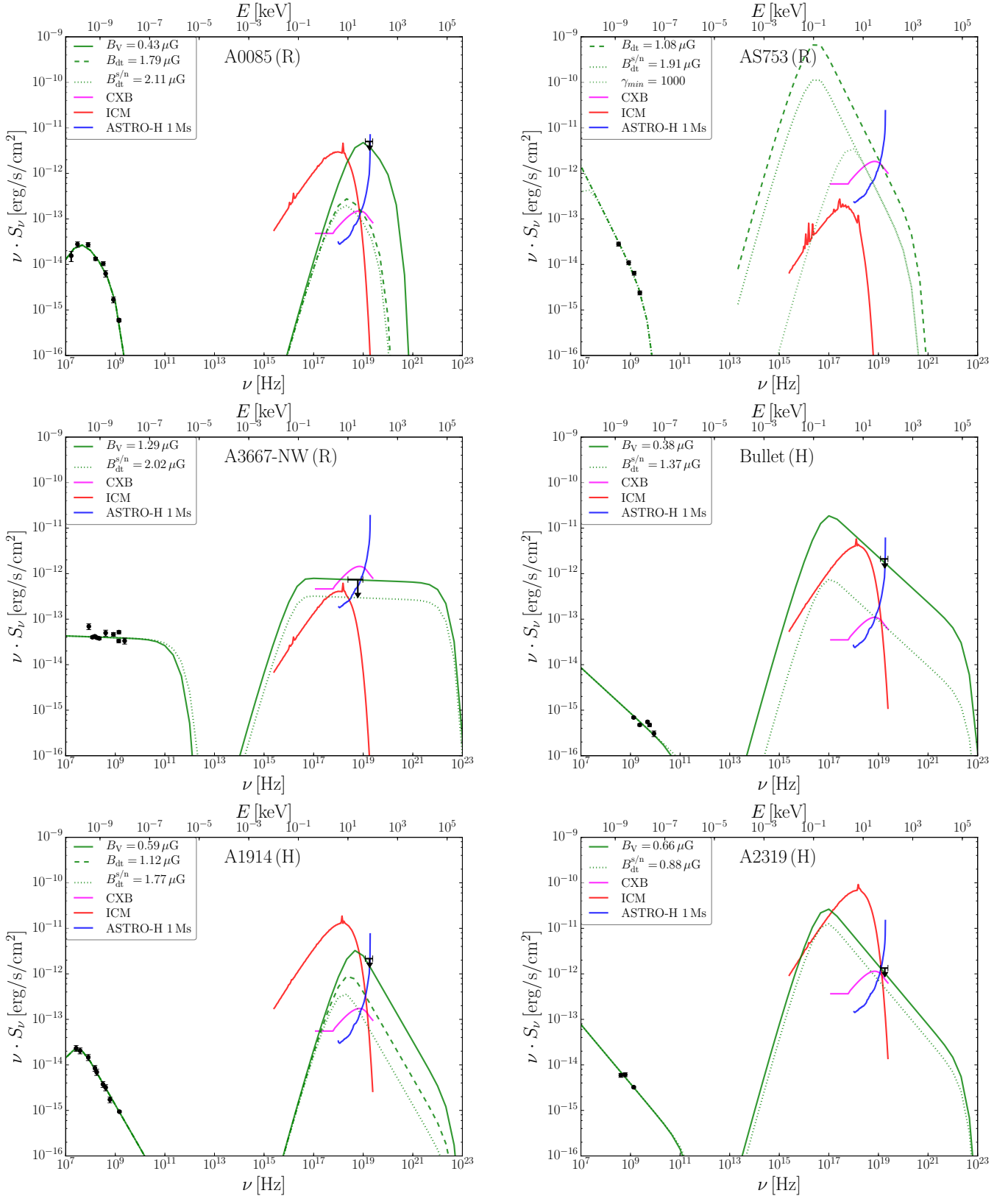


Fig. 3. Synchrotron and IC modelling of the A0085, AS753, and A3667-NW radio relics (R), and of the Bullet, A1914 and A2319 radio halos (H). Caption as in Fig. 2. For A3667-NW and A2319, the lines corresponding to B_{dt} are not shown as they correspond to that of B_V .

A3667. This cluster hosts the prototype double relic system (Rottgering et al., 1997). The 1.9 Mpc northwestern relic contains most of the diffuse emission. HXR emission from the A3667-NW relic has been studied by Ajello et al. (2009) and

Nakazawa et al. (2009). We use the latter upper limit on the HXR non-thermal emission since it specifically refers to the relic region. In addition, a detailed X-ray study of the ICM can be found in Finoguenov et al. (2010) and Akamatsu et al. (2012). We show

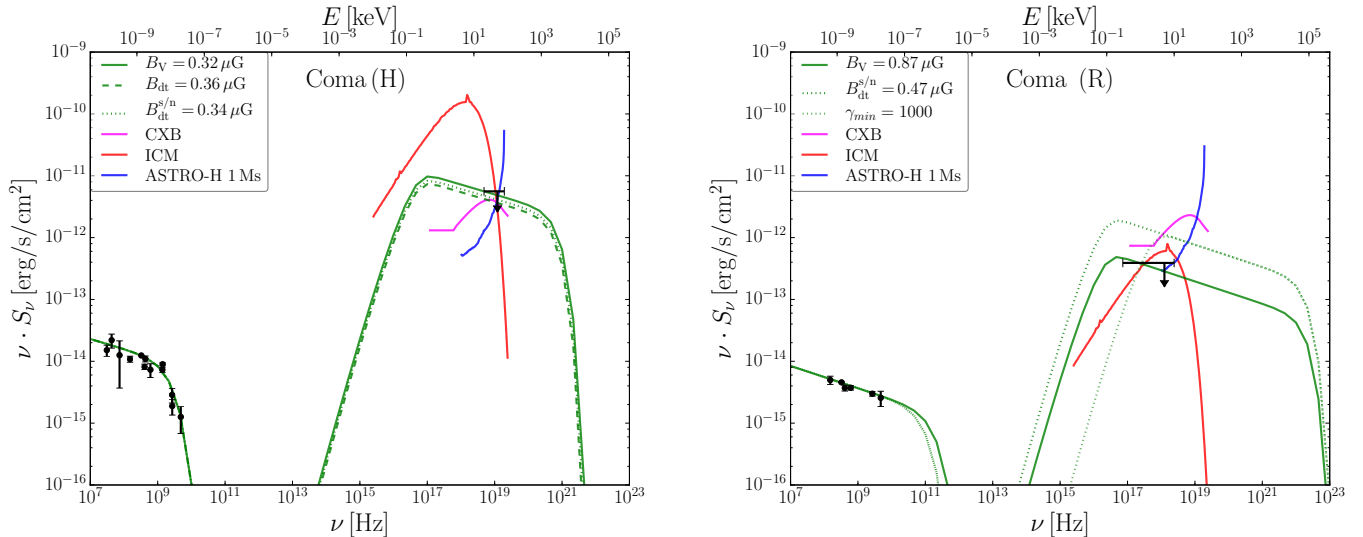


Fig. 4. Synchrotron and IC modelling of the radio halo (H) and relic (R) hosted by Coma. Caption as in Fig. 2. In the case of the relic, we do not show the line corresponding to B_{dt} because it gives worst estimates than that of B_V . This is due to our assumption of uniform radio sources which is particularly inappropriate in case of objects with a large size in the sky, like Coma. See main text for details.

the corresponding synchrotron and IC modelling in the central-left panel of Figure 3. The current HXR upper limit is at the same level of our B_{dt} prediction due to our assumption of uniform radio sources. We try to assess this issue in Table 7 providing an alternative estimate by assuming that all the radio emission comes from a region within the ASTRO-H HXI FoV.

Recently, Kitayama et al. (2014) pointed out that the A3667-NW relic is one of the more promising targets for ASTRO-H to detect non-thermal HXR emission. They predict that HXI can constrain the magnetic field to $B \geq 4 \mu\text{G}$ in 200 ks of observations. This is significantly higher, about a factor of two, than our predicted values of Tables 5 and 7. However, their approach is quite different as they estimate the 90% confidence-level (CL) upper limit obtainable with ASTRO-H in 200 ks of observations. Moreover, the discrepancy is mostly due to the fact that they assume that the SXR observed by Finoguenov et al. (2010) with XMM-Newton is of non-thermal origin, a hypothesis that cannot be excluded, and extrapolate this to HXRs with a power-law spectrum with a photon index of $\alpha = 2$.

Bullet. We include the Bullet cluster for the broad interest in it, and because it has been recently observed by NuSTAR, even if it does not fulfil our criteria to be in the promising targets list. Wik et al. (2014) recently reported the results of the NuSTAR observations of the Bullet cluster where they do not find any evidence of non-thermal HXR emission from the radio halo. We derive slightly better prospects for ASTRO-H than their derived upper limit as can be seen in the central-right panel of Fig. 3. Although ASTRO-H and NuSTAR have comparable performance in HXR, the former has the advantage of the simultaneous operation of the SXI, allowing for a better determination of the thermal ICM emission.

A1914. The radio halo of A1914 has a very steep spectrum (Bacchi et al., 2003; Komissarov & Gubanov, 1994). Note that while we modelled the low-energy flattening in radio with a spectral cutoff, the data is insufficient to distinguish it from a broken power-law, as can be seen in the bottom-left panel of Fig. 3. In this sense, therefore, the result of signal-to-noise approach should be taken with caution as it assumes a straight power-law in the 20–80 keV range, while some spectral features

could be expected. The X-ray upper limit is from Ajello et al. (2010).

A2255. This cluster hosts both a radio halo and a relic (Feretti et al., 1997). Since the relic is at $\sim 10'$ from the cluster centre and the XMM-Newton FoV is $30'$, current HXR upper limits likely contain contributions from both the halo and the relic (Turner et al., 2001; Wik et al., 2012). The synchrotron and IC emission modelling of the radio halo is shown in Figure 2. Note that while we use radio observations from Feretti et al. (1997) and Govoni et al. (2005), more recent observations were performed by Pizzo & de Bruyn (2009). However, considering the different areas used for the flux extraction, the latter results are comparable with the former for the purpose of our modelling.

A2319. We use the HXR upper limit from Ajello et al. (2009) and note that we obtain a more constraining lower limit $B_V > 0.7 \mu\text{G}$ due to our assumptions regarding the magnetic field distribution (see Sect. 4). The bottom-right panel of Figure 3 shows the corresponding synchrotron and IC modelling. The current HXR upper limit is at the same level of our B_{dt} prediction due to our assumption of uniform radio sources, where we try to assess this issue in Table 6 providing an alternative estimate by assuming that all the radio emission comes from a region within the ASTRO-H HXI FoV.

Coma. We included the Coma cluster more for *historical* reasons than for it being a real promising target. Coma is one of the best studied clusters and hosts the prototype radio halo and relic (e.g., Thierbach et al., 2003; Brown & Rudnick, 2011). A HXR excess at the halo location was claimed by Rephaeli & Gruber (2002) and Fusco-Femiano et al. (2004), but later never confirmed (Wik et al., 2009, 2011; Gastaldello et al., 2015). The radio relic (1253+275) is located at $75'$ from the cluster centre. Fig. 4 shows the synchrotron and IC modelling for both the radio halo and relic.

Note that, for the relic, the current upper limit (Feretti & Neumann, 2006) appears more constraining than what is achievable with ASTRO-H HXI in 1 Ms of observation according to the signal-to-noise analysis. However, this upper limit is determined in the 20 – 80 keV band and could be evaded with a low-energy spectral cutoff or flattening. Therefore, as for AS753, we

Table 8. Magnetic field equipartition estimates

Cluster	$B_{\text{eq}} (\mu\text{G})$	$B_{\text{eq}}^{\text{rev}} (\mu\text{G})$	Reference
Halos			
Bullet		1.2	1
A0520	1.4		2
A0665	0.6		3
A0754	0.7		4
Coma	0.5	0.7-1.9	1, 5, 6, 21
A1914	0.6	1.3	1, 4
A2163	0.7	1.0	1, 3
A2219	0.4	0.7	7
A2255	0.5		8
A2256	> 1	1.1	1, 9
A2319	0.5		10
A2744	0.5	1.0	1, 7
A3562	0.4		11
MACSJ0717.5+3745	3.4	6.5	12
RXCJ2003.5-2323		1.7	13
Relics			
Toothbrush		7.4-9.2	14
A0085	1.1-2.4		15, 20
A0754	0.3		15
AS753	1.3		15
A1240	N 1	2.4	16
	S 1	2.5	16
A1367	1		15
Coma	0.6	0.7-1.7	5, 6, 21
A1664	0.9		2, 17
A2163	2.2		22
A2255	0.5		8
A2256	> 1		9
A2345	E 0.8	2.2	16
	W 1	2.9	16
A2744	0.6	1.3	7
A3667	NW 1.5-2.5		6, 18
A4038	3		17
ZwCl0008.8-5215	E 2.5	6.6	19
ZwCl2341.1+0000	N 0.6	0.6	23
	E 0.5	0.7	23

Notes. Magnetic field estimates based on the equipartition theorem. B_{eq} is the equipartition magnetic field, while $B_{\text{eq}}^{\text{rev}}$ is the so-called revised equipartition magnetic field.

References.

(1) Petrosian et al. (2006); (2) Govoni et al. (2001); (3) Feretti et al. (2004); (4) Bacchi et al. (2003); (5) Giovannini et al. (1991); (6) Govoni & Feretti (2004); (7) Orru et al. (2007); (8) Feretti et al. (1997); (9) Clarke & Ensslin (2006); (10) Feretti et al. (1997); (11) Venturi et al. (2003); (12) Pandey-Pommier et al. (2013); (13) Giacintucci et al. (2009); (14) van Weeren et al. (2012); (15) Chen et al. (2008); (16) Bonafede et al. (2009b); (17) Kale & Dwarakanath (2012); (18) Johnston-Hollitt (2004); (19) van Weeren et al. (2011b); (20) Ensslin et al. (1998); (21) Thierbach et al. (2003); (22) Feretti et al. (2001).

also show the case with $\gamma_{\text{min}} = 1000$ in the right panel of Fig. 4. Also in the case of the halo, the current HXR upper limit is at the same level of our predictions for B_{dt} . This is due to our assumption of uniform radio sources which is particularly inappropriate in case of objects with a large size in the sky, like Coma. In fact, in Tables 6 and 7, we try to assess this issue providing alternative estimates by i) assuming that all the radio emission comes from a region within the ASTRO-H HXI FoV (we show this also for few other objects), and ii) computing the thermal ICM emission for the case of the halo only within the halo boundaries (we nor-

mally integrate over the full halos size, but again, due to the large sky size of Coma, here the difference is appreciable).

Kitayama et al. (2014) recently discussed the prospects for 500 ks of ASTRO-H observation of the halo region. They estimate a corresponding 90%CL upper limit of $B \sim 0.4 \mu\text{G}$, slightly more optimistic than our estimates, where, however, they assumed a photon index of $\alpha = 2$.

9. Conclusions

In this work, we modelled the synchrotron and IC emission of all known radio halos and relics for which the spectral index can be determined. Our approach is phenomenological towards the generation mechanism of relativistic electrons. We simply assume that the same electrons generating the observed radio synchrotron emission are responsible for HXR IC emission, where we adopt a power-law distribution with low- and high-energy cutoffs that we either fit to the radio data, if steepening is observed, or we fix to theoretically motivated values.

We provide updated lower limits on the magnetic field values for those objects for which an HXR upper limit is available. Subsequently, by considering the thermal ICM and CXB emissions, and the instrumental background, we provide predictions for the volume-average magnetic field values up to which HXR IC emission can be detected by the ASTRO-H HXI instrument, adopting different approaches and considering different observations times.

Our first approach is to estimate the magnetic field testable by ASTRO-H by taking as reference the intersection point between the dominant background emission, either thermal ICM or CXB, and the properly scaled ASTRO-H sensitivity for 1 Ms of observations. We then adopt a more robust approach based on photon counts in the 20 – 80 keV regime, requiring the signal-to-noise ratio to be higher than 5, where the noise includes the ICM and CXB emissions, and the instrumental background. With this approach, on which we base our conclusions, we estimate the magnetic field values testable by ASTRO-H in 100 ks, 500 ks and 1 Ms of observations. In this latter case, we find that the observation time needed to test a certain magnetic field value B roughly scales as $B \propto T_{\text{obs}}^{1/(2(1+\alpha))}$.

We identify as promising all those halos and relics for which the magnetic field testable by ASTRO-H in 100 ks is larger than $1 \mu\text{G}$ or than the equipartition estimates, where available. We provide the corresponding list of 15 halos and relics in Table 9. Among the most promising targets, we have the AS753 and A3667-NW relics, and the A2255 and A2319 halos, with an extension in the sky of the same order or larger than the ASTRO-H HXI FoV. Additionally, we can also identify as very promising the A0085, A2048 and A2063 relics, and the A1914 halo, with an extension smaller than the HXI FoV. The size in the sky of the considered object plays a crucial role in such observations, both for evaluating the contribution of the thermal ICM emission to the observed spectrum, and to plan multiple pointings with a corresponding increase in observation time.

We stress that we provide a theoretical expectation suffering from several approximations that we discuss openly in the text. While we estimate that most of these approximations imply conservative results, some of them could go in the other direction. In particular, the uncertainty in the ICM density distribution of some objects, particularly for radio relics in the clusters' outskirts, and the assumption of a power-law distribution of electrons down to low energies that are not tested by current radio observations, but could be tested soon by LOFAR. Therefore,

Table 9. Promising targets for ASTRO-H observations

Cluster	Source	Type	z	Size	α	$B_{\text{dt}}^{s/n}$ (100 ks)	$B_{\text{dt}}^{s/n}$ (1 Ms)	B_{dt} (1 Ms)	B_{eq}	$B_{\text{eq}}^{\text{rev}}$
Bullet		H	0.30	19	1.5	0.84	1.37	1.00		1.2
Toothbrush ^a		R	0.23	18	1.1	1.08	1.95	1.65		7.4-9.2
A0013 ^a		R	0.09	5	2.3	1.10	1.63	1.98		
A0085		R	0.06	26	1.6	1.33	2.11	1.79	1.1-2.4	
AS753 ^a		R	0.01	318	2.1	1.30	1.91	1.08	1.3	
Coma		H	0.02	710	1.2	0.20	0.34	0.36	0.5	0.7-1.9
		R		400	1.2	0.27	0.47	0.28	0.6	0.7-1.7
A1914		H	0.17	30	1.9	1.18	1.77	1.12	0.6	1.3
A2048 ^a		R	0.10	7	2.3	1.41	2.08	2.43		
A2063		R	0.03	3	1.2	2.25	4.12	5.51		
A2255		H	0.08	79	1.6	0.61	0.96	0.60	0.5	
A2319		H	0.06	198	1.7	0.56	0.88	0.65	0.5	
A3667	NW	R	0.06	250	1.0	1.12	2.02	0.94	1.5-2.5	
PLCK G287.0+32.9 ^a	N	R	0.39	7	1.3	0.77	1.35	1.57		
	S	R	0.39	6	1.5	1.05	1.75	4.14		

Notes. We summarise all objects that meet the criteria to be considered promising targets (see main text for details) and the corresponding magnetic field values testable by ASTRO-H in 100 ks and 1 Ms of observations in μG . We show the most optimistic values obtained adopting the signal-to-noise approach, $B_{\text{dt}}^{s/n}$, and also the more pessimistic estimates based on the intersection point between the background emission and the ASTRO-H sensitivity, B_{dt} , for 1 Ms of observations. We indicate the type of source, either radio halo (H) or radio relic (R), and, in case more than one relic is present in a given cluster, we explicitly mention to which source we are referring to. We also report the approximate surface on the sky in arcmin² and the spectral index α . Finally, we also show (revised) equipartition estimates, in μG , where available. ^(a) Thermal ICM emission computed using the model by Zandanel et al. (2014) for the gas density.

while it is clear that detailed ASTRO-H observation simulations should be performed to select the best target among the ones we propose here, in particular against their angular dimension in the sky, we conclude that HXR IC detection could be at hand for ASTRO-H in several objects.

Concluding, with the operation of NuSTAR and the upcoming launch of ASTRO-H, we will eventually be able to probe HXR IC emission in clusters for magnetic fields $\geq 1 \mu\text{G}$. Although detailed observation simulation are needed case by case, for a few clusters we might finally break the degeneracy between the magnetic field and the relativistic electrons distribution, and be able to shed new light on the non-thermal phenomena in clusters of galaxies.

Acknowledgements. We thank the anonymous referee for helping improving our manuscript. We thank Hiroki Akamatsu, Madoka Kawaharada, Matteo Murgia, Anders Pinzke, Jacco Vink and Franco Vazza for useful comments and discussions. We also profited from the Radio Observation of Galaxy Clusters database, collected by Klaus Dolag. This work was supported by the Netherlands Organization for Scientific Research (NWO) through a Veni and a Vidi grant (FZ and SA).

References

- Ajello, M., Rebusco, P., Cappelluti, N., et al. 2009, *ApJ*, 690, 367
Ajello, M., Rebusco, P., Cappelluti, N., et al. 2010, *ApJ*, 725, 1688
Akamatsu, H., de Plaa, J., Kaastra, J., et al. 2012, *PASJ*, 64, 49
Arnaud, K. A. 1996, in *Astronomical Society of the Pacific Conference Series*, Vol. 101, *Astronomical Data Analysis Software and Systems V*, ed. G. H. Jacoby & J. Barnes, 17
Bacchi, M., Feretti, L., Giovannini, G., & Govoni, F. 2003, *A&A*, 400, 465
Bagchi, J., Enßlin, T. A., Miniati, F., et al. 2002, *New A*, 7, 249
Bagchi, J., Sirothia, S. K., Werner, N., et al. 2011, *ApJ*, 736, L8
Barrena, R., Girardi, M., Boschin, W., & Dasi, M. 2009, *A&A*, 503, 357
Beck, R. & Krause, M. 2005, *Astronomische Nachrichten*, 326, 414
Blumenthal, G. R. & Gould, R. J. 1970, *Rev. Mod. Phys.*, 42, 237
Böhringer, H. & Werner, N. 2010, *A&A Rev.*, 18, 127
Bonafede, A., Brügggen, M., van Weeren, R., et al. 2012, *MNRAS*, 426, 40
Bonafede, A., Feretti, L., Giovannini, G., et al. 2009a, *A&A*, 503, 707
Bonafede, A., Feretti, L., Murgia, M., et al. 2010, *A&A*, 513
Bonafede, A., Giovannini, G., Feretti, L., Govoni, F., & Murgia, M. 2009b, *A&A*, 494, 429
Bonafede, A., Vazza, F., Brügggen, M., et al. 2013, *MNRAS*, 433, 3208
Boschin, W., Girardi, M., & Barrena, R. 2013, *MNRAS*, 434, 772
Brentjens, M., A. 2008, *A&A*, 489, 69
Brown, S., Duesterhoeft, J., & Rudnick, L. 2011, *ApJ*, 727, L25
Brown, S. & Rudnick, L. 2011, *MNRAS*, 412, 2
Brunetti, G. 2003, in *Astronomical Society of the Pacific Conference Series*, Vol. 301, *Matter and Energy in Clusters of Galaxies*, ed. S. Bowyer & C.-Y. Hwang, 349
Brunetti, G., Giacintucci, S., Cassano, R., et al. 2008, *Nature*, 455, 944
Brunetti, G. & Jones, T. W. 2014, *International Journal of Modern Physics D*, 23, 30007
Brunetti, G., Rudnick, L., Cassano, R., et al. 2013, *A&A*, 558, A52
Brunetti, G., Setti, G., & Comastri, A. 1997, *A&A*, 325, 898
Carilli, C. L. & Taylor, G. B. 2002, *ARA&A*, 40, 319
Cavagnolo, K. W., Donahue, M., Voit, G. M., & Sun, M. 2009, *ApJ*, 182, 12
Cavaliere, A. & Fusco-Femiano, R. 1976, *A&A*, 49, 137
Chen, C. M. H., Harris, D. E., Harrison, F. A., & Mao, P. H. 2008, *Monthly Notices of the Royal Astronomical Society*, 383, 1259
Chen, Y., Reiprich, T. H., Böhringer, H., Ikebe, Y., & Zhang, Y. Y. 2007, *A&A*, 466, 805
Clarke, T. E. 2004, *Journal of Korean Astronomical Society*, 37, 337
Clarke, T. E. & Ensslin, T. A. 2006, *astron. jour.*, 131, 2900
Cohen, A. S. & Clarke, T. E. 2011, *AJ*, 141, 149
Comastri, A., Setti, G., Zamorani, G., & Hasinger, G. 1995, *A&A*, 296, 1
Eckert, D., Produit, N., Paltani, S., Neronov, A., & Courvoisier, T. J.-L. 2008, *A&A*, 479, 27
Enßlin, T. A. 2002, *A&A*, 396, L17
Ensslin, T. A., Biermann, P. L., Klein, U., & Kohle, S. 1998, *A&A*, 332, 395
Ensslin, T. A. & Sunyaev, R. A. 2002, *A&A*, 383, 423
Enßlin, T. A. & Vogt, C. 2006, *A&A*, 453, 447
Feretti, L., Böhringer, H., Giovannini, G., & Neumann, D. 1997, *A&A*, 317, 432
Feretti, L., Fusco-Femiano, R., Giovannini, G., & Govoni, F. 2001, *A&A*, 373, 106
Feretti, L., Giovannini, G., & Böhringer, H. 1997, *New Astronomy*, 2, 501
Feretti, L., Giovannini, G., Govoni, F., & Murgia, M. 2012, *The Astronomy and Astrophysics Review*, 20, 1
Feretti, L. & Neumann, D. M. 2006, *A&A*, 450, L21
Feretti, L., Orru, E., Brunetti, G., et al. 2004, *A&A*, 423, 111
Feretti, L., Schuecker, P., Böhringer, H., Govoni, F., & Giovannini, G. 2005, *A&A*, 444, 157
Finoguenov, A., Sarazin, C. L., Nakazawa, K., Wik, D. R., & Clarke, T. E. 2010, *ApJ*, 715, 1143
Fukazawa, Y., Makishima, K., & Ohashi, T. 2004, *Publications of the Astronomical Society of Japan*, 56, 965

- Fusco-Femiano, R., Orlandini, M., Brunetti, G., et al. 2004, *ApJ*, 602, L73
- Gastaldello, F., Wik, D. R., Molendi, S., et al. 2015, *ApJ*, 800, 139
- Gavazzi, G. & Trinchieri, G. 1983, *ApJ*, 270, 410
- Giacintucci, S. 2011, *Mem. Soc. Astron. Italiana*, 82, 541
- Giacintucci, S., Dallacasa, D., Venturi, T., et al. 2011, *A&A*, 534
- Giacintucci, S., Kale, R., Wik, D. R., Venturi, T., & Markevitch, M. 2013, *ApJ*, 766, 18
- Giacintucci, S., Venturi, T., Brunetti, G., et al. 2005, *A&A*, 440, 867
- Giacintucci, S., Venturi, T., Brunetti, G., et al. 2009, *A&A*, 505, 45
- Gilli, R., Comastri, A., & Hasinger, G. 2007, *A&A*, 463, 79
- Giovannini, G., Bonafede, A., Feretti, L., et al. 2009, *A&A*, 507, 1257
- Giovannini, G. & Feretti, L. 2000, *New Astronomy*, 5, 335
- Giovannini, G., Feretti, L., & Stanghellini, C. 1991, *A&A*, 252, 528
- Govoni, F. & Feretti, L. 2004, *International Journal of Modern Physics D*, 13, 1549
- Govoni, F., Feretti, L., Giovannini, G., et al. 2001, *A&A*, 376, 803
- Govoni, F., Murgia, M., Feretti, L., et al. 2005, *A&A*, 430, L5
- Gruber, D. E. 1992, in *The X-ray Background*, ed. X. Barcons & A. C. Fabian, 44
- Harrison, F. A., Craig, W. W., Christensen, F. E., et al. 2013, *ApJ*, 770, 103
- Henriksen, M. & Mushotzky, R. 2001, *The Astrophysical Journal*, 553, 84
- Hindson, L., Johnston-Hollitt, M., Hurley-Walker, N., et al. 2014, *MNRAS*, 445, 330
- Johnston-Hollitt, M. 2004, in *The Riddle of Cooling Flows in Galaxies and Clusters of galaxies*, ed. T. Reiprich, J. Kempner, & N. Soker, 51
- Juett, A. M., Sarazin, C. L., Clarke, T. E., et al. 2008, *ApJ*, 672, 138
- Kale, R. & Dwarakanath, K. S. 2012, *ApJ*, 744, 46
- Kale, R., Dwarakanath, K. S., Bagchi, J., & Paul, S. 2012, *Monthly Notices of the Royal Astronomical Society*, 426, 1204
- Kassim, N. E., Clarke, T. E., Enßlin, T. A., Cohen, A. S., & Neumann, D. M. 2001, *ApJ*, 559, 785
- Kawano, N., Fukazawa, Y., Nishino, S., et al. 2009, *PASJ*, 61, 377
- Kempner, J. C. & Sarazin, C. L. 2001, *ApJ*, 548, 639
- Kitayama, T., Bautz, M., Markevitch, M., et al. 2014, *ArXiv:1412.1176*
- Komissarov, S. S. & Gubanov, A. G. 1994, *A&A*, 285, 27
- Liang, H., Hunstead, R. W., Birkinshaw, M., & Andreani, P. 2000, *ApJ*, 544, 686
- Lindner, R. R., Baker, A. J., Hughes, J. P., et al. 2014, *ApJ*, 786, 49
- Longair, M. 2011, *High Energy Astrophysics* (Cambridge University Press)
- Ma, C.-J., Ebeling, H., Donovan, D., & Barrett, E. 2008, *ApJ*, 684, 160
- Macario, G., Venturi, T., Intema, H. T., et al. 2013, *A&A*, 551
- Mantz, A., Allen, S. W., Ebeling, H., Rapetti, D., & Drlica-Wagner, A. 2010, *Monthly Notices of the Royal Astronomical Society*, 406, 1773
- Marini, F., Bardelli, S., Zucca, E., et al. 2004, *Monthly Notices of the Royal Astronomical Society*, 353, 1219
- Menanteau, F., Hughes, J. P., Sifón, C., et al. 2012, *ApJ*, 748, 7
- Million, E. T. & Allen, S. W. 2009, *Monthly Notices of the Royal Astronomical Society*, 399, 1307
- Molendi, S. & Gastaldello, F. 2009, *A&A*, 493, 13
- Mori, H., Maeda, Y., Ishida, M., et al. 2012, in *Society of Photo-Optical Instrumentation Engineers (SPIE) Conference Series*, Vol. 8443, Society of Photo-Optical Instrumentation Engineers (SPIE) Conference Series, 5
- Murgia, M., Eckert, D., Govoni, F., et al. 2010, *A&A*, 514, A76
- Murgia, M., Govoni, F., Feretti, L., et al. 2004, *A&A*, 424, 429
- Nakazawa, K., Sarazin, C. L., Kawahara, M., et al. 2009, *PASJ*, 61, 339
- Ogrean, G. A., Brüggén, M., van Weeren, R. J., et al. 2013, *Monthly Notices of the Royal Astronomical Society*, 433, 812
- Orru, E., Murgia, M., Feretti, L., et al. 2007, *A&A*, 467, 943
- Ota, N. 2012, *Research in Astronomy and Astrophysics*, 12, 973
- Ota, N., Nagayoshi, K., Pratt, G. W., et al. 2014, *A&A*, 562, A60
- Pacholczyk, A. 1970, *Radio Astrophysics: Nonthermal Processes in Galactic and Extragalactic Sources*, *Astronomy and Astrophysics Series* (W. H. Freeman)
- Pandey-Pommier, M., Richard, J., Combes, F., et al. 2013, *A&A*, 557
- Pérez-Torres, M. A., Zandanel, F., Guerrero, M. A., et al. 2009, *MNRAS*, 396, 2237
- Petrosian, V. 2001, *ApJ*, 557, 560
- Petrosian, V., Madejski, G., & Luli, K. 2006, *ApJ*, 652, 948
- Piffaretti, R., Arnaud, M., Pratt, G. W., Pointecouteau, E., & Melin, J. B. 2011, *A&A*, 534
- Pinzke, A., Pfrommer, C., & Bergström, L. 2011, *Physical Review D*, 84
- Pizzo, R., F. & de Bruyn, A., G. 2009, *A&A*, 507, 639
- Planck Collaboration, Ade, P. A. R., Aghanim, N., et al. 2014, *A&A*, 571, A29
- Popesso, P., Biviano, A., Böhringer, H., & Romaniello, M. 2007, *A&A*, 461, 397
- Reid, A. D., Hunstead, R. W., Lémonon, L., & Pierre, M. M. 1999, *Monthly Notices of the Royal Astronomical Society*, 302, 571
- Rephaeli, Y. 1979, *ApJ*, 227, 364
- Rephaeli, Y. & Gruber, D. 2002, *ApJ*, 579, 587
- Rephaeli, Y., Gruber, D., & Arieli, Y. 2006, *ApJ*, 649, 673
- Rephaeli, Y., Nevalainen, J., Ohashi, T., & Bykov, A. M. 2008, *Space Sci. Rev.*, 134, 71
- Röttgering, H., Afonso, J., Barthel, P., et al. 2012, *Journal of Astrophysics and Astronomy*, 557, 34
- Röttgering, H., van Weeren, R., Brüggén, M., et al. 2013, *Astronomische Nachrichten*, 334, 333
- Röttgering, H. J. A., Wieringa, M. H., Hunstead, R. W., & Ekers, R. D. 1997, *MNRAS*, 290, 577
- Sarazin, C. 1999, *ApJ*, 520, 529
- Sarazin, C. L. 1988, X-ray emission from clusters of galaxies
- Sarazin, C. L. & Lieu, R. 1997, *Astrophys.J.Lett.*
- Sehgal, N., Hughes, J. P., Wittman, D., et al. 2008, *ApJ*, 673, 163
- Shen, S., Kauffmann, G., Von Der Linden, A., White, S. D. M., & Best, P. N. 2008, *Monthly Notices of the Royal Astronomical Society*, 389, 1074
- Shimwell, T. W., Brown, S., Feain, I. J., et al. 2014, *MNRAS*, 440, 2901
- Slee, O. B., Roy, A. L., Murgia, M., Andernach, H., & Ehle, M. 2001, *AJ*, 122, 1172
- Smith, R. K., Brickhouse, N. S., Liedahl, D. A., & Raymond, J. C. 2001, *ApJ*, 556, L91
- Storm, E., Jeltama, T. E., & Rudnick, L. 2015, *MNRAS*, 448, 2495
- Stroe, A., Rumsey, C., Harwood, J. J., et al. 2014, *MNRAS*
- Subrahmanyan, R., Beasley, A. J., Goss, W. M., Golap, K., & Hunstead, R. W. 2003, *AJ*, 125, 1095
- Takahashi, T., Mitsuda, K., Kelley, R., et al. 2012, in *Society of Photo-Optical Instrumentation Engineers (SPIE) Conference Series*, Vol. 8443, Society of Photo-Optical Instrumentation Engineers (SPIE) Conference Series, 1
- Takahashi, T., Mitsuda, K., Kelley, R., et al. 2014, in *Society of Photo-Optical Instrumentation Engineers (SPIE) Conference Series*, Vol. 9144, Society of Photo-Optical Instrumentation Engineers (SPIE) Conference Series, 25
- Takahashi, T., Mitsuda, K., Kelley, R., et al. 2010, in *Society of Photo-Optical Instrumentation Engineers (SPIE) Conference Series*, Vol. 7732, Society of Photo-Optical Instrumentation Engineers (SPIE) Conference Series, 0
- Thierbach, M., Klein, U., & Wielebinski, R. 2003, *A&A*, 397, 53
- Turner, M. J. L., Abbey, A., Arnaud, M., et al. 2001, *A&A*, 365, L27
- Vacca, V., Feretti, L., Giovannini, G., et al. 2014, *A&A*, 561
- van Weeren, R. J., Bonafede, A., Ebeling, H., et al. 2012a, *MNRAS*, 425, L36
- van Weeren, R. J., Brüggén, M., Röttgering, H. J. A., et al. 2011a, *A&A*, 533
- van Weeren, R. J., Fogarty, K., Jones, C., et al. 2013, *ApJ*, 769, 101
- van Weeren, R. J., Hoefl, M., Röttgering, H. J. A., et al. 2011b, *A&A*, 528
- van Weeren, R. J., Röttgering, H. J. A., Intema, H. T., et al. 2012b, *A&A*, 546
- van Weeren, R. J., Röttgering, H. J. A., Bagchi, J., et al. 2009, *A&A*, 506, 1083
- van Weeren, R. J., Röttgering, H. J. A., Rafferty, D. A., et al. 2012, *A&A*, 543, A43
- van Weeren, R. J., Röttgering, H. J. A., H. J. A., & Brüggén, M. 2011c, *A&A*, 527
- Venturi, T., Bardelli, S., Dallacasa, D., et al. 2003, *A&A*, 402, 913
- Venturi, T., Giacintucci, S., Brunetti, G., et al. 2007, *A&A*, 463, 937
- Venturi, T., Giacintucci, S., Cassano, R., et al. 2009, in *Astronomical Society of the Pacific Conference Series*, Vol. 407, *The Low-Frequency Radio Universe*, ed. D. J. Saikia, D. A. Green, Y. Gupta, & T. Venturi, 232
- Vogt, C. & Enßlin, T. A. 2005, *A&A*, 434, 67
- Voit, G. M. 2005, *Reviews of Modern Physics*, 77, 207
- Wik, D. R., Hornstrup, A., Molendi, S., et al. 2014, *ApJ*, 792, 48
- Wik, D. R., Sarazin, C. L., Finoguenov, A., et al. 2011, *ApJ*, 727, 119
- Wik, D. R., Sarazin, C. L., Finoguenov, A., et al. 2009, *ApJ*, 696, 1700
- Wik, D. R., Sarazin, C. L., Zhang, Y.-Y., et al. 2012, *ApJ*, 748, 67
- Yoon, J. H., Schawinski, K., Sheen, Y.-K., Ree, C. H., & Yi, S. K. 2008, *ApJS*, 176, 414
- Zandanel, F., Pfrommer, C., & Prada, F. 2014, *Monthly Notices of the Royal Astronomical Society*, 438, 116

Appendix A: Other figures and comments on individual clusters

This appendix contains the figures for the synchrotron and IC modelling of all clusters not shown in the main text. For some of these, the IC emission peaks in SXR or EUV above the CXB and ICM emissions, and we, therefore, also show the case with $\gamma_{\min} = 1000$.

Note that several objects, mainly radio relics, have the peculiarity of a very low thermal ICM emission, probably an underestimation by observations pointed to the cluster's center, or due to the use of the phenomenological model of

Zandanel et al. (2014) for the gas density. In some cases (A0781, A2163, MACSJ1149,5-2223-E and W, MACSJ1752.0+4440-SW, PLCK G287.0+32.9-N and S), the CXB dominates over the thermal ICM emission, and, additionally, the intersection point between the ASTRO-H and CXB emissions is at an energy lower than the rise in the CXB spectrum. The corresponding results for B_{dt} should be taken with caution and, in fact, in these cases, the signal-to-noise approach gives more conservative, and reasonable, results.

We also remind the reader that the signal-to-noise approach is done assuming a straight power-law in the 20 – 80 keV energy band (see Sect. 7). While in most cases the cutoffs are at much lower and higher energies, for A2063 and A0013 this method could give slightly optimistic results.

All figures can be read as explained in the caption of Fig. 2.

